

High-Voltage Systems and Dielectric Materials

Academic and Research Staff

Professor Markus Zahn

Visiting Scientists and Research Affiliate

Qing Yang

Graduate Students

George Hwang, Jouya Jadidian, Xuewei Zhang

The RLE/LEES/HVRL High-Voltage Systems and Dielectric Materials Research Group pursues theoretical and experimental investigations in high voltage conduction and breakdown phenomena.

1. Mechanisms Behind Positive Streamers and Their Distinct Propagation Modes in Transformer Oil

Sponsors

This work was supported by ABB Corporate Research, Vasteras, Sweden via the MIT Energy Initiative and the National Science and Engineering Research Council of Canada.

Project Staff

George Hwang, Jouya Jadidian, and Markus Zahn

Introduction

The widespread use of dielectric liquids for high voltage insulation and power apparatus cooling is due to their greater electrical breakdown strength and thermal conductivity than gaseous insulators, while their ability to conform to complex geometries and self-heal means that they are often of more practical use than solid insulators. Unfortunately, as with all insulation, the failure of liquid insulation can cause catastrophic damage to not only the power equipment, but also the surrounding environment. Furthermore, failure often leads to major operational disruption and financial loss for the failed equipment's owner.

Due to the major implications of insulation failure in electric power apparatus, scientists and engineers have for many years studied the insulating properties of dielectric liquids, particularly transformer oils, trying to understand the mechanisms behind electrical breakdown in an effort to reduce the likelihood of breakdown [1]-[3]. Much of this work has focused on the formation of electrical streamers. These are low density conductive structures that form in regions of oil that are over-stressed by electric fields on the order of 1×10^8 V/m or greater [2]. Once a streamer forms, it tends to elongate, growing from the point of initiation towards a grounding point. The extent of a streamer's development depends upon the nature of the electrical excitation (*i.e.*, magnitude, duration, rise time, etc.) which caused it. Sustained over-excitation can result in a streamer short circuiting the oil gap between electrodes. When this happens an electric breakdown arc will form.

The important role which streamers play in the electrical breakdown of dielectric liquids has meant that they have been the subject of significant scientific investigation. Much of the research on streamers in transformer oil has been empirical in nature and has led to the formation of a large literature on the subject of which the references [1]-[9] are representative. Unfortunately, unlike the gaseous and solid states, the molecular structure and behavior of liquids is more complex and even in the purest liquids there exists trace amounts of impurities that make it difficult to isolate the mechanisms behind electrical breakdown [8],[9]. In particular, transformer oil is a mixture of many different aromatic, naphthenic, and paraffinic molecules with complex molecular structures.

With the advancement of measurement technologies over the past several decades, the quantity and quality of experimental results has increased significantly. The material in the literature generally reports on the qualitative physical characteristics of streamers (*i.e.*, shape, velocity, light emission, etc.) under various experimental conditions, along with detailing their voltage and current dynamics. This material

provides very useful insight into pre-breakdown processes in transformer oil, allowing researchers to develop better models to understand streamers. For example, researchers have observed experimentally that streamers have propagation characteristics that are strongly dependent on the voltage excitation to the liquid [1]-[7]. In the case of transformer oil, experimental evidence has shown that for positive streamers having a high probability (*i.e.*, greater than 50%) of leading to breakdown tend to initiate at a lower applied voltage magnitude and propagate faster and further than similar high-energy negative streamers [1],[3]. As a result, high-energy positive streamers constitute a greater risk to oil insulated high voltage electrical equipment than do negative streamers and are the focus of this work.

Other key observations regarding streamers in transformer oil are the existence of four distinct positive streamer propagation modes, called the 1st, 2nd, 3rd, and 4th modes, for lightning impulse voltage excitations in transformer oil. The onsets of the four modes are dependent on the magnitude of the excitation with the 1st mode initiating at the lowest voltage magnitude and the 4th mode at the highest. In pre-breakdown studies, the 1st mode is often ignored as the probability of breakdown occurring is low. Moreover, 1st mode streamers have a bush-like structure and propagate at velocities on the order of 100 m/s [10], well below the speed of sound in oil. The slow 2nd mode initiates slightly below the breakdown voltage V_b , which denotes 50% probability of breakdown, and dominates up until the acceleration voltage V_a [7]. These streamers are filamentary in shape with several main branches [4],[7]. Near the acceleration voltage, the streamer propagation transitions to the fast 3rd mode where the propagation velocity rises dramatically and the streamer shape is more branched [7]. With a slight increase in applied voltage above the acceleration voltage, the streamer propagation quickly changes to the fast event 4th mode, which is extremely filamentary with one or two main branches [4],[7]. Therefore, with increased applied voltage, the streamer velocity and shape changes dramatically, such that the 1st, 2nd, 3rd, and 4th modes propagate with velocities on the order of 0.1 km/s, 1 km/s, 10 km/s, and 100 km/s, respectively [3]-[7].

The transition from the 2nd to 3rd mode, which occurs near the acceleration voltage V_a , is of great importance because 3rd mode streamers propagate at extremely fast velocities such that they quickly traverse the oil gap to the cathode before the applied voltage impulse can be extinguished causing electrical breakdown. Biller [11] hypothesized that for non-homogeneous dielectric liquids like transformer oil, the propagation of slow mode streamers is linked to the ionization of the “easily ionizable” molecules in the liquid, while the faster modes result from the ionization of the main “ordinary” molecules. In the context of transformer oil, the easily ionizable species are equivalent to aromatic molecules which generally have lower ionization energy potentials [12],[13] and lower number density [14],[15] than the naphthenic and paraffinic molecules. The ordinary molecules are precisely the main naphthenic and paraffinic hydrocarbons that comprise the majority of transformer oil.

The literature contains a handful of postulated charge generation mechanisms that result in streamer propagation. Several commonly hypothesized charge generation mechanisms are electric field dependent ionic dissociation (the Onsager Effect) [16],[17], Fowler-Nordheim electron injection from the cathode [2], vaporization [17], collisional ionization [18], and electric field dependent molecular ionization [9], [19]-[1]. The scope of this paper will focus on the fast mechanisms which occur in the bulk of transformer oil that lead to positive filamentary streamer formation where the timescales of interest are in the nanosecond to microsecond range. Therefore, slowly propagating bush-like streamers (*i.e.*, less than the speed of sound in transformer oil ~ 1.4 km/s) and breakdown caused by other phenomena such as gassing and trapped voids are not discussed [23],[24].

In the first half of this work a mathematical model is developed, based upon the local field and hydrodynamic approximations, to investigate streamer development in transformer oil. The models are solved numerically using the finite element software package COMSOL Multiphysics [25]. Using plausible parameters for the model, the numerical results fit experimental data reasonably well to suggest that field ionization is an important mechanism in streamer development in transformer oil.

The second half of this work utilizes the developed model to explain the mechanisms and conditions that produce various streamer propagation modes in transformer oil, in particular the slow 2nd and fast 3rd mode filamentary positive streamers. The results show that the qualitative model by Biller [11] accurately describes the underlying physics that leads to different streamer modes in transformer oil.

This summary extends the streamer modeling and results of [21] by analyzing the effects of ionizing various molecular species on streamer propagation. The new results corroborate Biller's hypothesis regarding the development of slow and fast streamers on the ionization of low concentration, low ionization potential molecules and high concentration, high ionization potential molecules, respectively. Furthermore, this categorization of molecules lends well to transformer oil that is comprised of low concentration, low ionization potential aromatic molecules and high concentration, high ionization potential naphthenic/paraffinic molecules. Also, a preliminary model is presented based on earlier electrohydrodynamic stability analysis that predicts streamer protrusion spacing in transformer oil.

Mathematical Model and System Geometry

The governing equations that contain the physics to model streamer development are based on the drift-dominated charge continuity equations (2)-(4) for positive ion (ρ_p), negative ion (ρ_n) and electron (ρ_e) charge densities which are coupled to Gauss' Law (1). The negative ion and electron densities are both negative quantities. The three carrier continuum model is utilized to account for the charge generation and capture mechanisms, which are critical in the study of streamers.

$$\nabla \cdot (\epsilon \vec{E}) = \rho_p + \rho_n + \rho_e \quad (1)$$

$$\frac{\partial \rho_p}{\partial t} + \nabla \cdot (\rho_p \mu_p \vec{E}) = G_I(|\vec{E}|) + \frac{\rho_p \rho_e R_{pe}}{q} + \frac{\rho_p \rho_n R_{pn}}{q} \quad (2)$$

$$\frac{\partial \rho_n}{\partial t} - \nabla \cdot (\rho_n \mu_n \vec{E}) = \frac{\rho_e}{\tau_a} - \frac{\rho_p \rho_n R_{pn}}{q} \quad (3)$$

$$\frac{\partial \rho_e}{\partial t} - \nabla \cdot (\rho_e \mu_e \vec{E}) = -G_I(|\vec{E}|) - \frac{\rho_p \rho_e R_{pe}}{q} - \frac{\rho_e}{\tau_a} \quad (4)$$

To check the correctness of signs in equations (2)-(4), conservation of charge requires that the sum of the right-hand sides of equations (2)-(4) must be zero.

In equations (1)-(4), μ_p , μ_n and μ_e are the mobilities of the positive ions ($1 \times 10^{-9} \text{ m}^2 \text{V}^{-1} \text{s}^{-1}$), negative ions ($1 \times 10^{-9} \text{ m}^2 \text{V}^{-1} \text{s}^{-1}$) and electrons ($1 \times 10^{-4} \text{ m}^2 \text{V}^{-1} \text{s}^{-1}$) respectively. Also, ϵ is the oil's permittivity ($2.2\epsilon_0$). In the time scales of interest for streamer formation, that is nanoseconds to microseconds, the oil's velocity is negligible such that no effects of fluid convection are included in equations (2)-(4). q is the magnitude of electronic charge ($1.602 \times 10^{-19} \text{ C}$) and \vec{E} is the local electric field. τ_a is the electron attachment time constant to neutral molecules. R_{pn} and R_{pe} are the ion-ion and ion-electron recombination rates, respectively, in transformer oil. G_I is the electric field dependent molecular ionization rate, which is discussed in detail.

Due to the high field levels and accompanying large particle velocities, especially the electrons, the large particle convection leads to instability in the numerical solver. Therefore, artificial streamline diffusion is employed to avoid spurious oscillations in the solutions to the convection equations (2)-(4) and assist in solver stability [26]. While there are other numerical methods to obtain more accurate solutions, such as

the finite difference or finite element methods with flux-corrected transport technique [27], the use of artificial diffusion is adequate for transformer oil streamer modeling [28].

The setup corresponds to the needle-sphere electrode geometry as shown in Figure 1 and detailed in the IEC 60897 standard [29]. The axial distance between the needle electrode's tip and the spherical electrode is 25 mm. The radius of curvature of the needle electrode and spherical electrode are 40 μm and 6.35 mm, respectively. The applied voltage to the needle electrode is a step voltage. The model

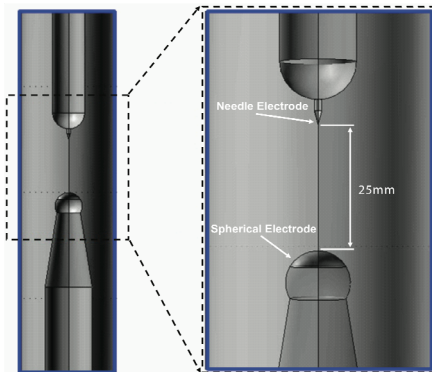
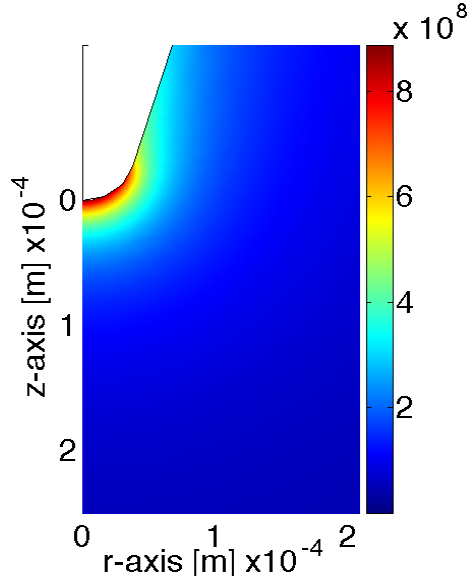
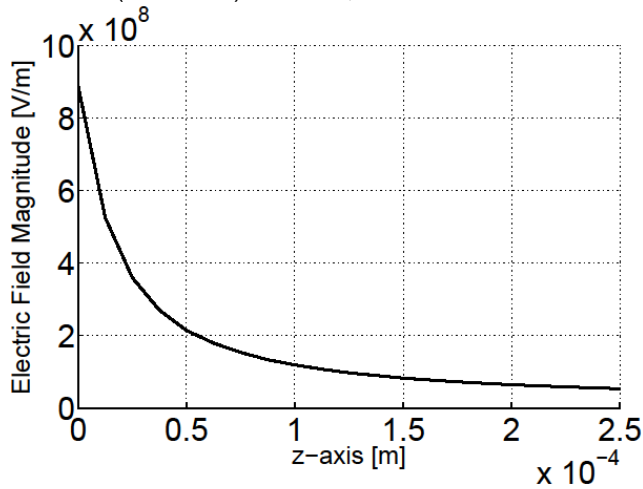


Figure 1. Computer-aided design representation of the needle-sphere electrode geometry used for streamer simulation purposes.



(a) 2D axisymmetric Laplacian electric field magnitude [V/m] spatial distribution (*i.e.*, $\nabla \cdot (\partial \vec{E}) = 0$) for 300 kV applied voltage near the 40 μm radius needle electrode apex at the origin. The nearest point of the sphere electrode (not shown) is at $r = 0$, $z = 25$ mm.



(b) Laplacian electric field magnitude distribution along the needle-sphere z -axis. The field enhancement is greatest near the sharp needle tip and quickly decreases as z increases.

Figure 2. Laplacian electric field magnitude for 300 kV applied voltage to the 40 μm needle tip electrode.

$$W = \frac{3q_e^2}{20\pi\epsilon_0 R_e} \quad (5)$$

Einstein's theory of relativity tells us that the work necessary to assemble the charge is stored as energy that is related to the mass as $W = m_e c^2$ where c is the speed of light in free space. Equating the two expressions results in an expression for the electron radius as

equations (1)-(4) are solved in their two-dimensional axisymmetric form.

Application of a 300 kV step voltage to the needle electrode creates a non-uniform Laplacian electric field distribution at $t = 0^+$ with a large field enhancement near the sharp needle tip as shown in the electric field magnitude distribution plots of Figure 2. Due to the non-uniform field enhancement near the needle tip, the main activity and dynamics at times immediately after zero are localized in the needle tip region. Note that at later times (*i.e.*, $t > 0^+$) the electric field near the needle tip decreases due to charge generation and injection, becoming space charge limited.

Carrier Mobility

Transformer oil is not a pure liquid hydrocarbon, but is a mixture of various naphthenic, paraffinic, and aromatic molecules with a complex molecular structure. The various molecules that comprise transformer oil make it difficult to characterize many parameters, such as charge carrier mobility. The electron mobility in transformer oil, to the authors' best knowledge, has not been well characterized. This is partially due to the reason stated above, as well as the varying sources, types, and distributors of transformer oil. In this work, an educated estimate of the electron mobility in transformer oil is based upon the logarithmic average of the electron mobility of common hydrocarbons. Generally, the electron mobility in these liquids range from $1 \times 10^{-6} \text{ m}^2 \text{V}^{-1} \text{s}^{-1}$ to $1 \times 10^{-2} \text{ m}^2 \text{V}^{-1} \text{s}^{-1}$ [30],[31]. Therefore, the electron mobility in transformer oil was chosen as $1 \times 10^{-4} \text{ m}^2 \text{V}^{-1} \text{s}^{-1}$ in this work.

A method to validate this choice for electron mobility in transformer oil is via the classical electron radius, known as the Lorentz radius, as calculated in [32],[33]. The electron is modeled as a small, uniformly charged spherical volume with charge density ρ_0 and radius R_e with total charge $q_e = 4\pi R_e^3 \rho_0 / 3$ within a medium with a dielectric permittivity ϵ . The total work needed to assemble the electron sphere is [32]

$$R_e = \frac{3q_e^2}{20\pi\epsilon m_e c^2}. \quad (6)$$

For the case of an electron ($q = -e = -1.6 \times 10^{-19}$ C, $m_e = 9.1 \times 10^{-31}$ kg) in transformer oil ($\epsilon = 2.2\epsilon_0$), the radius is $R_e = 7.66 \times 10^{-16}$ m. Now using Walden's rule for a spherical particle, the electron mobility is

$$\mu_e = \frac{q}{6\pi\eta R_e} = 5.5 \times 10^{-4} \text{ m}^2 \text{V}^{-1} \text{s}^{-1}, \quad (7)$$

where $\eta = 0.02$ Pa/s is a representative value for the viscosity of transformer oil. This result, while based upon classical methods, can be viewed as a first-order approximation to the electron mobility and has helped select the value of $\mu_e = 1 \times 10^{-4} \text{ m}^2 \text{V}^{-1} \text{s}^{-1}$. However the electron mobility is a key parameter in dictating streamer propagation velocity and as such the velocity is sensitive to this value. On the other hand, streamer development, ignoring velocity, is quite insensitive to electron mobility as long as it is approximately two orders of magnitude greater than the positive ion mobility. This is because the electrons must be sufficiently fast enough to exit the ionization zone to create a narrow space charge region, which results in electric field enhancement in the oil as will be discussed in Section 3.

Regarding the positive ion and negative ion mobility values in transformer oil, the ion mobility values of $\mu_p = 1 \times 10^{-9} \text{ m}^2 \text{V}^{-1} \text{s}^{-1}$ has been verified experimentally for transformer oil by Gáfvert *et al.* [34]. It is also in agreement with the analysis of Adamczewski [23].

Recombination and Electron Attachment

The Langevin-Debye relationship [34],[35] is used to model ion-ion R_{pn} and ion-electron R_{pe} recombination rates in transformer oil. According to the Langevin-Debye relationship, the recombination rates can be expressed as

$$R_{pn} = \frac{q(\mu_p + \mu_n)}{\dot{\phi}}, \quad (8)$$

$$R_{pe} = \frac{q(\mu_p + \mu_e)}{\dot{\phi}}. \quad (9)$$

The ion-electron recombination rate of equation (9) is overestimated because the Langevin-Debye relationship is valid for situations where the electric field levels are low to moderate and the recombining species are of similar physical scale [35]. This recombination model overestimates the rate of ion-electron recombination in liquids at low to moderate electric field levels [36],[37]. To compensate for the reduction in the recombination cross-section caused by high electric field levels, some authors have used the Langevin-Debye recombination term for ion-ion recombination, R_{pn} , to model ion-electron recombination, R_{pe} [38]. This approach effectively compensates for the reduction in the recombination cross-section by reducing the apparent electron mobility. Using the respective value for each variable (*i.e.*, ion mobilities equal to $1 \times 10^{-9} \text{ m}^2 \text{V}^{-1} \text{s}^{-1}$) the recombination rates are $R_{pn} = R_{pe} = 1.64 \times 10^{-17} \text{ m}^3/\text{s}$.

In addition to recombination, electrons also attach to neutral molecules to form negative ions. This process is modeled as an electron attachment time constant, $\tau_a = 200$ ns [20],[38].

Electric Field Dependent Molecular Ionization

During streamer formation, the generation and movement of free charge carriers, such as ions and electrons, in the dielectric liquid results in significant thermal dissipation, which leads to the liquid-to-gas phase change. Therefore, any attempt to understand streamer development in electrically stressed dielectric liquids must focus on uncovering the dominant charge generation mechanisms.

The complex nature and structure of liquids has inhibited the development of a comprehensive liquid state theory. Rather, scientists have derived models and a basic understanding of processes in liquids by utilizing theories from both the solid-state [39],[40] and compressed gas-state [2]. In regards to the modeling and understanding of pre-breakdown phenomena in liquids, the liquid modeled as a compressed gas most often prevails with scientists taking concepts from gas discharge physics [24],[41]. This inherently has to do with the development of a low-density gaseous-phase during streamer formation

and the ease in which the transition between phases occurs with varying temperature and pressure [2]. However, streamers in liquids show several phenomenological similarities to electrical trees in solids, and the comparison of liquids and amorphous solids has found some promising results [42]-[44].

Electric field dependent ionization, also known as field ionization, is a direct ionization mechanism which has its origins from solid-state theory [9],[45]. It is an ionization process whereby an extremely high electric field results in the elevation of a valence band electron in a neutral molecule to the conduction band, thus generating both a free positive ion and a free or quasi-free electron. Field ionization as a free charge carrier generation source in dielectric liquids such as transformer oil has often been discussed in the literature from a qualitative standpoint [9],[19],[47],[48]. Halpern and Gomer [49] were the first to show the existence of field ionization as a free charge carrier generation mechanism in cryogenic liquids. Their work spurred other researchers to validate experimentally field ionization in other insulating liquids [50],[51].

In their ground breaking work, Devins, Rzaev, and Schwabe [9] applied the Zener model for field ionization to dielectric liquids to explain streamer propagation. In this work, the field ionization charge density rate is [45]

$$G_i(|\vec{E}|) = \frac{q^2 n_0 a |\vec{E}|}{h} \exp\left(-\frac{\pi^2 m^* a \Delta^2}{qh^2 |\vec{E}|}\right) \quad (10)$$

where h is Planck's constant, a is the molecular separation distance, m^* is the effective electron mass, n_0 is the number density of ionizable species and Δ is the liquid-phase ionization potential.

Modeling Families of Molecules

The major difficulty in trying to apply equation (10) to transformer oil is determining correct parameter values. Many commonly used dielectric liquids, such as transformer oil, are comprised of numerous individual molecular species, each with unique number density, ionization potential, and mass. Also, values for molecular separation distance, effective electron mass, and ionization potential are not well characterized for molecules in the liquid-state. In these cases, educated assumptions are made based upon known liquid-state characteristics and the chemical composition of saturated and unsaturated hydrocarbons.

For example, a typical hydrocarbon liquid has a molecular number density on the order of $1 \times 10^{27} \text{ m}^{-3}$ to $1 \times 10^{28} \text{ m}^{-3}$, of which only a small percentage are ionized [15]. The molecular separation distance is strictly a solid-state concept and is difficult to find an analogous measure in liquids, however Qian *et al.* [38] state that the molecular separation distance of water is $3.0 \times 10^{-10} \text{ m}$ and Beroual and Tobazeon [52] use a value of $5.0 \times 10^{-10} \text{ m}$ in their analyses. In non-polar liquids, scientists have found that the effective electron mass can also be below the free electron mass m_e , and it generally ranges from $0.1 \times m_e$ to m_e [53],[54]. Lastly, the ionization potential of hydrocarbon liquids and gases ranges from $9.6 \times 10^{-19} \text{ J}$ to $1.92 \times 10^{-18} \text{ J}$ (6 eV to 12 eV) [9],[12],[13],[31].

Commercial transformer oil contains two main groups of hydrocarbons, the trace aromatic molecules and the main high density naphthenic or paraffinic molecules [14]. Due to their chemical composition and structure, aromatic molecules generally have lower ionization potentials than naphthenic/paraffinic molecules making them easier to ionize [12],[13],[31]. However, due to the high number density of naphthenic/paraffinic molecules in transformer oil, if enough energy were to be supplied to ionize these molecules a greater amount of free charge would be produced. To study the conditions and effects of charge generation due to each molecule type, recalling Biller's hypothesis relating streamer modes and different molecules [11], the two following cases are examined in this paper:

- i. Aromatic molecules with low ionization potential and low number density,
- ii. Naphthenic/paraffinic molecules with high ionization potential and high number density.

Representative number density and ionization potential parameters for aromatic and naphthenic/paraffinic molecules used in this study are summarized in Table 1, where the effective electron mass and molecular separation distance were chosen to be the same for both types. The ionization potentials are $\Delta=9.60 \times 10^{-19}$ J (6.00 eV) which correspond to common aromatic molecules and $\Delta=1.58 \times 10^{-18}$ J (9.86 eV) which correspond to the naphthenic molecules such as cyclohexane [13], a well characterized and discussed hydrocarbon used in many streamer empirical studies [55],[56].

Case 1: Aromatic Hydrocarbon Molecules

The numerical results to the streamer model equations (1)-(4) for the field ionization mechanism of equation (10) with parameter values corresponding to the low concentration and easily ionizable aromatic hydrocarbon molecules in Table 1 are presented in this section. The applied step voltage to the needle electrode is $V_{app} = 100$ kV. In Figure 3, the electric field and net space charge density distributions along the needle-sphere symmetry z-axis are shown at several instances in time. In Figure 4, the rz -plane spatial distribution of the electric field magnitude at the same instances in time are shown.

Figure 3a and 3b show significant temporal dynamics in the electric field and space charge density distributions with peaks in the profile occurring further out in the oil volume as time progresses and away from the positive applied voltage at the sharp needle electrode. Field ionization produces positive ions and electrons in the oil that travel in opposite directions, with the positive ions and electrons attracted to the grounded electrode and positively excited needle electrode, respectively. However, due to the relatively high mobility of the electrons ($\mu_e = 1 \times 10^{-4} \text{ m}^2 \text{V}^{-1} \text{s}^{-1}$) compared to the large positive ions ($\mu_p = 1 \times 10^{-9} \text{ m}^2 \text{V}^{-1} \text{s}^{-1}$), the newly generated electrons quickly exit the high field ionization zone towards the anode, leading to the development of a net positive space charge peak as shown in Figure 3b for several different times.

The peaks in space charge density distribution are a source of electric field. The superposition of the space charge and the Laplacian electric fields generate a total electric field with a field enhancement (Figure 3a) at the space charge peak (Figure 3b) that drives field ionization and streamer propagation further into the oil. The peak electric field in the oil is approximately 3.5×10^8 V/m. The results suggest that field ionization of low concentration, easily ionizable aromatic hydrocarbon molecules plays an important role in the development and propagation of positive streamers in transformer oil.

In addition to examining temporal dynamics along the needle-sphere z-axis, the spatial distribution of the electric field gives insight into streamer dynamics. From Figure 4a, at early times, the electric field enhancement is localized near the sharp needle electrode due to the applied voltage. As time progresses, an extremely large field enhancement occurs further out in the oil (Figure 4b). At even later times, the electric field distribution shows a cylindrical-like streamer that is centered along the z-axis (Figure 4c, 4d, 4e). The cylindrical streamer is enveloped by a field enhancement at the cylinder's boundary, with the greatest enhancement occurring at the streamer tip that is furthest away from the needle electrode. This point of greatest field enhancement is exactly the largest electric field peak in Figure 3a.

By approximating the dimensions of the streamer to be equal to the volume enclosed by the electric field enhancement, the radius of the streamer near the field enhanced streamer tip is 5-10 μm . The average streamer velocity, as it travels along the z-axis, is 3.0 km/s after 100 ns.

Case 2: Naphthenic/Paraffinic Hydrocarbon Molecules

The numerical results to the streamer model equations (1)-(4) for the field ionization mechanism of equation (10) with parameter values corresponding to the high concentration and high ionization potential naphthenic/paraffinic hydrocarbon molecules comprising the base of transformer oil in Table 1 are

Table 1. Case studies: parameter values for aromatic and naphthenic/paraffinic molecules.

Parameter	Symbol	Case 1: Aromatic	Case 2: Naphthenic/Paraffinic	Reference
Number density	n_0	$1 \times 10^{23} \text{ m}^{-3}$	$1 \times 10^{26} \text{ m}^{-3}$	[11],[14],[15]
Ionization potential	Δ	$9.60 \times 10^{-19} \text{ J}$ (6.00 eV)	$1.58 \times 10^{-18} \text{ J}$ (9.86 eV)	[12],[13]
Molecular separation	a	$3.0 \times 10^{-10} \text{ m}$	$3.0 \times 10^{-10} \text{ m}$	[38],[52]
Effective electron mass	m^*	$0.1 \times m_e = 9.11 \times 10^{-32} \text{ kg}$	$9.11 \times 10^{-31} \text{ kg}$	[53],[54]

presented in this section. The applied voltage to the needle electrode is increased to $V_{app} = 300$ kV, which is needed to ionize the higher ionization potential molecules. In Figure 5 the electric field and net space charge density distributions along the needle-sphere symmetry z-axis are shown at several instances in time. In Figure 6, the rz-plane spatial distribution of the electric field magnitude is shown.

The macroscopic streamer results for the high concentration, high ionization potential molecules are similar to the low concentration, low ionization potential case in Case1. In particular, the generation of free positive ions and electrons due to field ionization of high concentration, high ionization potential molecules leads to significant temporal dynamics in the electric field and space charge (Figure 5a and 5b). This results in the development of electric field and space charge enhancements in the oil volume that occur further away from the needle electrode as time progresses. As in the case of low concentration, low ionization potential molecules, the results suggest that field ionization of the high concentration, high ionization potential naphthenic/paraffinic molecules is a possible key contributor to the development and propagation of positive streamers in transformer oil.

The qualitative results are similar for the low concentration, low ionization potential molecules (Case 1) and the high concentration, high ionization potential molecules; however, on closer inspection, the two cases differ quantitatively in the electric field and space charge density values. For example, the maximum of the electric field peak in the oil is approximately 7×10^8 V/m (Figure 5a) which is about double that for the low concentration, easily ionizable molecules of Case 1 (Figure 3a).

There is also a significant increase in the space charge density compared to the results of Case 1. This results from the ionization of high concentration, high ionization potential molecules creating more space charge. The higher field level is partially due to the application of a higher applied voltage, 300 kV rather than the 100 kV for the low concentration, easily ionizable molecules; however, higher field level is also strongly related to the significantly greater space charge levels that contribute to the electric field. The higher applied voltage is required to ionize the high concentration molecules comprising the base liquid due to their increased ionization potential (Table 1).

From the spatial distribution of the electric field (Figure 6), the electric field enhancement is localized near the sharp needle electrode at early times; however, it quickly travels further out into the oil at short times afterwards. Unlike for Case 1, the low concentration, easily ionizable molecules case, the electric field distribution for the ionization of the high concentration, high ionization potential molecules show a conical-like streamer that is centered along the z-axis and travels more quickly across the electrode gap. The conical streamer is enveloped by a field enhancement at the cone's boundary, with the greatest enhancement at the streamer tip that is furthest away from the needle electrode. This point of greatest field enhancement is exactly the electric field peak in Figure 5a.

Approximating the dimensions of the streamer to be equal to the volume enclosed by the electric field enhancement, the radius of the streamer channel near the field enhanced streamer tip is approximately $1.0 \mu\text{m}$. The average streamer velocity, as it travels along the z-axis is 9.5 km/s after 100 ns. Interestingly, the streamer at times after $t = 50$ ns has protrusions from the main streamer body that look similar to streamer branch filaments. Due to computational limitations, the model is restricted to a two-dimensional axisymmetric model simplification, where there is no ϕ -dependence. As such, these protrusions are actually conical in shape rather than the true branched filaments that are experimentally observed. Examining these protrusions, it was first assumed that they appeared due to numerical instability; however the protrusions continued to exist upon greater levels of discretization. Therefore, while the protrusions in Figure 6 are truly conical, they are modeled as protrusions of a cylindrical jet resulting from electrohydrodynamic instability in the next section.

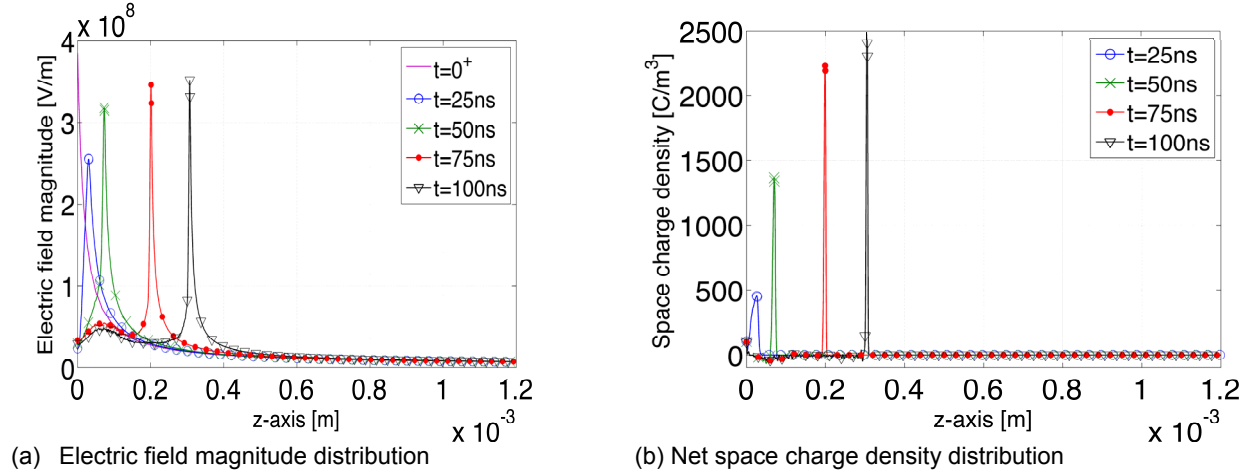


Figure 3. Temporal dynamics along the needle-sphere electrode axis at 25 ns intervals from $t = 25$ -100 ns given by the solution to the streamer model equations (1)-(4) for an applied step voltage of $V_{app} = 100$ kV and a low concentration of easily ionizable molecules with parameter values summarized in Table 1. Note, at time $t = 0^+$ the electric field distribution represents the Laplacian electric field.

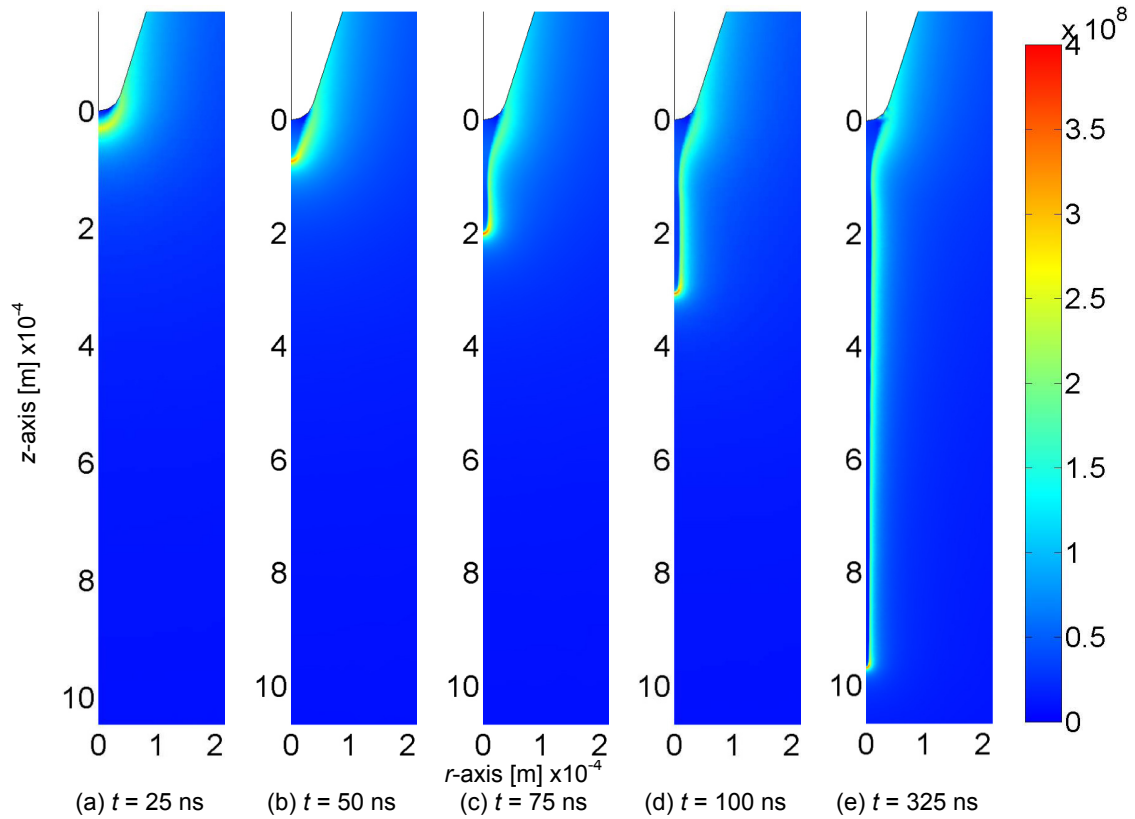


Figure 4. Electric field magnitude [V/m] spatial distributions (as a function of r and z in the electrode geometry) from $t = 25$ -325 ns given by the solution to the streamer model equations (1)-(4) for an applied step voltage of $V_{app} = 100$ kV and a low concentration of easily ionizable molecules with parameter values summarized in Table 1.

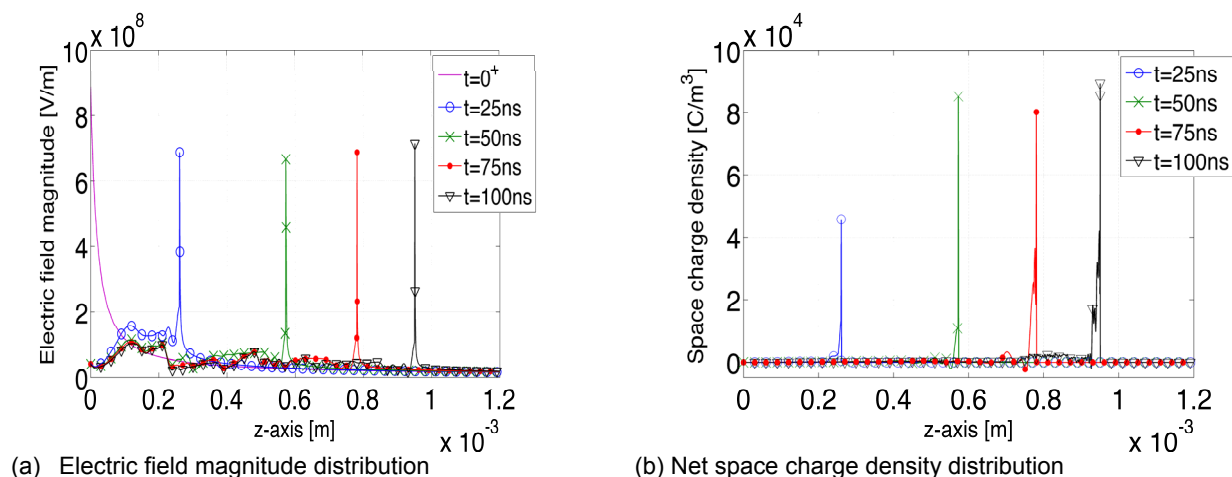


Figure 5. Temporal dynamics along the needle-sphere electrode axis at 25 ns intervals from $t = 25$ -100 ns given by the solution to the streamer model equations (1)-(4) for an applied step voltage of $V_{app} = 300$ kV and a high concentration, high ionization potential molecules with parameter values summarized in Table 1. Note, at time $t = 0^+$ the electric field distribution represents the Laplacian electric field.

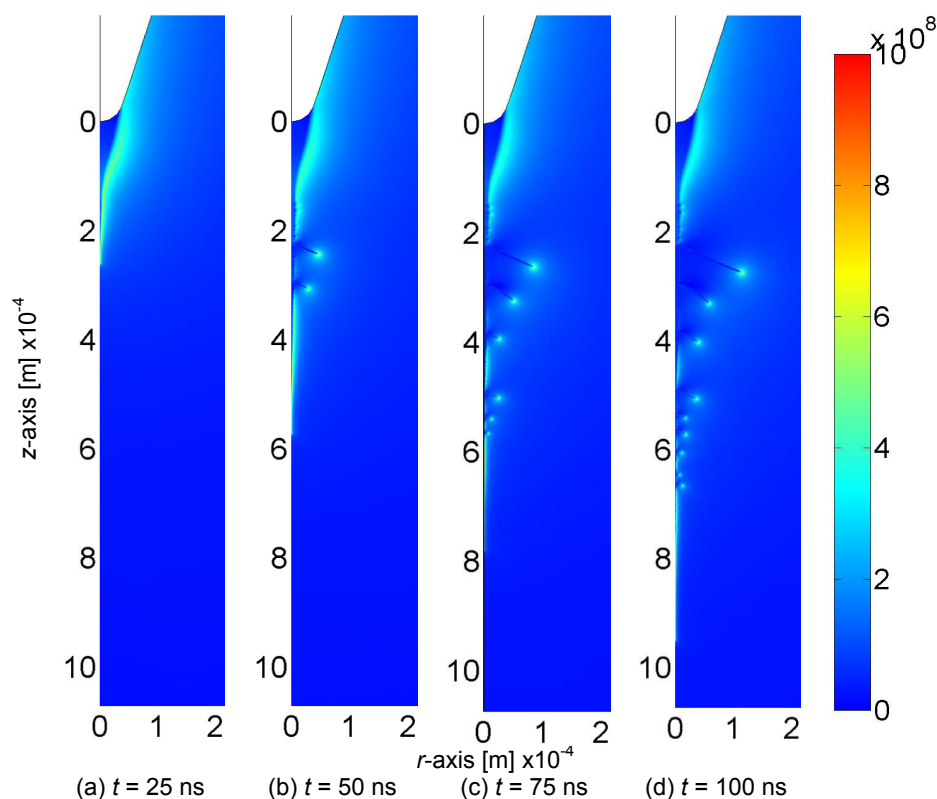


Figure 6. Electric field magnitude [V/m] spatial distributions (as a function of r and z in the electrode geometry) from $t = 25$ -100 ns given by the solution to the streamer model equations (1)-(4) for an applied step voltage of $V_{app} = 300$ kV and high concentration, high ionization potential molecules with parameter values summarized in Table 1. Note the streamer radial protrusions in Figures 6(b)-6(d) which resemble streamer branching that may be due to electrohydrodynamic instability.

Preliminary Model for Streamer Protrusions

We propose a preliminary model of the streamer protrusions in Figure 6 as being due to an electrohydrodynamic instability of a uniform volume charged filled jet of radius R , surface tension γ , and charge density Q as developed in references [57]-[59]. For simplicity, we emphasize space charge effects by assuming that the jet and the surrounding oil have the same dielectric permittivity ϵ so that there are no polarization forces on the jet interface. Linear small signal radial perturbations $\xi(\theta, z, t)$ of the cylindrical interface from $r=R$ are of the form

$$\xi(\theta, z, t) = \text{Re} \left\{ \hat{\xi} \exp[j(\omega t - m\theta - kz)] \right\} \quad (11)$$

where $j = \sqrt{-1}$. Applying the boundary conditions of continuity of potential, displacement, normal component of electric field, and force balance as given by Eqs. (52)-(54) in Ref. [58] and by Eqs. (34)-(35) in Ref. [59] give the system dispersion relation as

$$\left(\frac{\omega}{\omega_j} \right)^2 = -(kR)^2 I'_m(kR) K'_m(kR) \{ (kR)^2 + m^2 - 1 - Q_j^2 [0.5 - I_m(kR) K_m(kR)] \} \quad (12)$$

where

$$\begin{aligned} (\omega_j)^2 &= \frac{\gamma}{\rho R^3}, & (Q_j)^2 &= \frac{Q^2 R^3}{\partial \gamma}, \\ I'_m(kR) &= \frac{d[I_m(kR)]}{d[kR]}, & K'_m(kR) &= \frac{d[K_m(kR)]}{d[kR]}. \end{aligned} \quad (13)$$

$I_m(kR)$ and $K_m(kR)$ are respectively the modified Bessel functions of the first and second kind of order m .

The charged jet radius is stable in time if ω is real as then $|\xi(\theta, z, t) / \hat{\xi}| < 1$ and is unstable when ω has a negative imaginary part as then $\xi(\theta, z, t)$ in (11) will grow exponentially with time. We hypothesize that such unstable growth for small displacements of $\xi(\theta, z, t)$ become large signal non-linear growth that result in the protrusions seen in Figure 6.

Figure 6 of Ref. [58] non-dimensionally plots $(\omega/\omega_j)^2$ versus kR in Eq. (12) considering kR real and allowing $(\omega/\omega_j)^2$ to be positive because with ω real the streamer is stable as represented by the positive part of each plot. With $(\omega/\omega_j)^2$ negative ω is imaginary and the streamer is unstable. For our simulations in Figure 6 we have found or chosen representative parameter values as $Q \approx 300 \text{ C/m}^3$, $R \approx 1 \text{ }\mu\text{m}$, $\epsilon = 2.2\epsilon_0$, $\rho \approx 880 \text{ kg/m}^3$, $\gamma \approx 0.004 \text{ Nt/m}$ to give $\omega_j \approx 2 \times 10^6 \text{ rad/s}$ and $Q_j^2 \approx 1.1$.

For this value of Q_j^2 we examine Figure 6 of Ref. [58] and see that modes $m = 2$ and 3 are stable as those modes result in real values of ω . For mode $m = 0$, approximate values of $0.2 < kR < 0.9$ are unstable. This range corresponds to a wavelength range of approximately $7 < \lambda/R < 30$. The peak unstable frequency magnitude is about $0.2\omega_j$ corresponding to a growth time constant of about $2.5 \text{ }\mu\text{s}$. For $m=1$, the unstable wavenumber range is $0 < kR < 0.35$ corresponding to the wavelength range $\lambda/R > 18$. The peak unstable frequency magnitude is about $0.1\omega_j$ corresponding to a growth time constant of about $5 \text{ }\mu\text{s}$. With $R = 1 \text{ }\mu\text{m}$ we thus expect $m=1$ protrusions with spacing greater than $18 \text{ }\mu\text{m}$ with exponential growth rate of order $5 \text{ }\mu\text{s}$ and $m=0$ protrusions in the range of 7 to $30 \text{ }\mu\text{m}$ with exponential growth rate of order $2.5 \text{ }\mu\text{s}$.

In Figure 6 of the present paper we note protrusion spacings of order 20 - $100 \text{ }\mu\text{m}$ with a growth rate of order 36 ns . Thus our speculative instability analysis is in the right range for protrusion periodicity but predicts a slower growth rate than appears in the calculations of Figure 6. A more refined space charge instability analysis will better fully examine the instability analyses of references [57]-[59] which also include polarization forces. It might be expected that the streamer being a low density region might have a dielectric constant closer to that of free space than that of transformer oil. The polarization force might further destabilize the cylindrical interface causing the instability to grow faster.

Field Ionization of Various Oil Molecules

The results of Cases 1 and 2 demonstrate that field ionization of differing families of molecules drives the development and propagation of distinct filamentary positive streamers in transformer oil. Figure 3a and

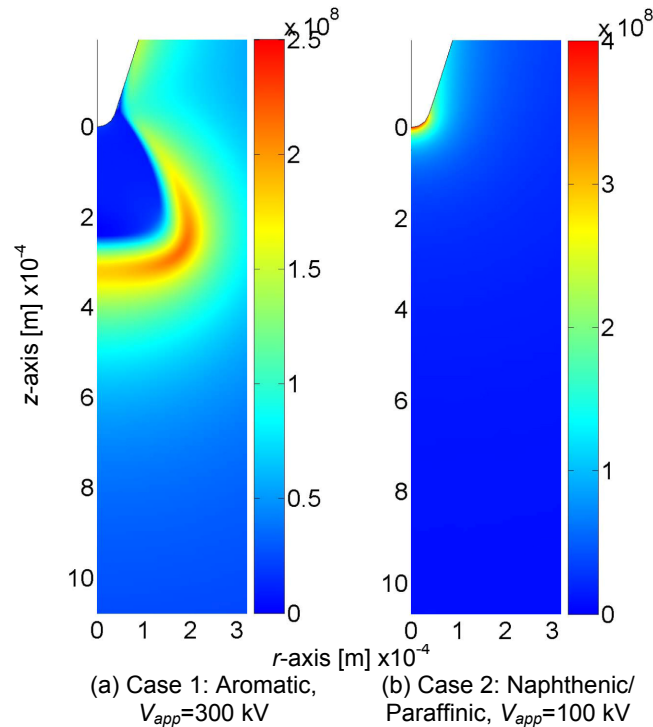


Figure 7. Electric field magnitude [V/m] spatial distributions (as a function of r and z in the electrode geometry) at time $t = 100$ ns given by the solution to the streamer model equations (1)-(4). Note the different scales for the color bars in (a) and (b).

5a show that for both the low concentration, easily ionizable molecule and high concentration, high ionization potential molecule cases that significant temporal dynamics in the electric field distribution occur in the oil volume between the needle tip and spherical electrode. The peak of the electric field does not occur at the needle tip, as it does for the Laplacian field (Figure 2), but rather at a point in the oil gap between the two electrodes. This temporally dynamic electric field distribution represents an ionizing electric field wave that ionizes molecules into slow positive ions and fast electrons.

There are major differences in the streamers produced by the ionization of low concentration, easily ionizable molecules to those developed from the ionization of high concentration, high ionization potential molecules comprising the base liquid. A key difference in the models of Cases 1 and 2 is that the applied step voltage to the needle electrode, V_{app} , was 100 kV and 300 kV, respectively. This selection was not arbitrary, rather applying $V_{app}=100$ kV to the high concentration, high ionization potential molecules of Case 2 results in no streamer formation, as shown in Figure 7b, due to their higher ionization potential compared to their low concentration, easily ionizable

counterparts (see Table 1). Also, applying $V_{app}=300$ kV to the low concentration, easily ionizable molecules, as in Figure 7a, results in a streamer with similar propagation velocity along the z -axis and field enhancement levels as those presented for Case 1, where $V_{app}=100$ kV (Figure 4d). However, the streamer of Figure 7a is branched wider in the radial direction.

Verifying Biller's Qualitative Model for Streamer Propagation Modes

The key characteristics of the streamers Case 1, which are generated due to the ionization of low concentration, easily ionizable molecules, closely resemble slow 2nd mode filamentary positive streamers in transformer oil. In particular, their propagation velocity (3.0 km/s), electric field peak ($\sim 4 \times 10^8$ V/m), radial dimension (10 μ m), and breakdown inception voltage for the 25 mm needle-sphere geometry (~ 100 kV) match the empirical data from several research groups [3]-[7],[42],[60]. Also, Figure 7 showed that with increased applied voltage, the streamer expanded greatly in the radial direction; however, its axial growth was not significant. This phenomenon is characteristic of slow 2nd mode streamers in transformer oil that have an increasingly branched structure with greater applied voltage; however, their velocity stays relatively constant [4],[7].

The streamers of Case 2, which are generated due to the ionization of high concentration, high ionization potential molecules, resemble fast 3rd mode branched filamentary positive streamers in transformer oil. Their propagation velocity (10 km/s), electric field peak ($\sim 1 \times 10^9$ V/m), radial dimension (1 μ m), and inception voltage for the 25 mm gap needle-sphere geometry (~ 300 kV) match the empirical data from several research groups [3]-[7],[42],[60]. The fast 3rd mode streamer inception voltage is equivalent to the acceleration voltage, where the streamer propagation velocity increases an order of magnitude from 2-5 km/s for slow 2nd mode streamers to 10-20 km/s for fast 3rd mode streamers [7],[60]. Consequently, high concentration, high ionization potential molecules are not ionized at the lower voltages, as shown in Figure 7b for $V_{app}=100$ kV, for which the low concentration, easily ionizable molecules are significantly ionized.

The simulations capture the interdependence between streamer radius and the maximum level of electric field enhancement reported by researchers such as Beroual and Tobazeon [52]. They keenly observed an inverse relationship between streamer radius and maximum field level, where as the streamer radius decreased as the maximum field level at the streamer tip increased. In Section 3.1, the ionization of the low concentration, low ionization potential molecules resulted in a streamer with larger radius but lower field enhancement than that of the streamer resulting from the high concentration, high ionization potential molecules in Section 3.2. This is non-intuitive because in the latter case there is a high concentration of ionizable molecules and a high enough applied voltage ($V_{app} = 300$ kV) to ionize them; however, the ionization zone is small. Consequently, this results in the space charge being concentrated in a small volume leading to greater field enhancement and ionization and ultimately faster streamer propagation.

The ability to ionize low or high number density molecules is related directly to the amount of space charge created in the ionization region. Ionizing the high concentration, high ionization potential molecules creates more space charge (Figure 5b) compared to the low concentration, easily ionizable molecules (Figure 3b). Consequently a larger electric field enhancement is produced at the streamer tip that allows for a more efficient field ionization (*i.e.*, higher $G_r(\vec{E})$). The resulting streamer is of the fast 3rd mode type. While several researchers have obtained data that suggests that streamer velocity is inversely proportional to the liquid density [9],[52], these studies focused on slow bush-like positive (and negative) streamers that traveled at velocities below the speed of sound, where different mechanisms may be at work. Therefore, those results are not directly applicable to this study.

Conversely, the ionization of the lower concentration, easily ionizable aromatic molecules in transformer oil generates space charge levels that lead to lower field enhancement. This field enhancement level is too low to ionize high potential naphthenic/paraffinic molecules such that only slower 2nd mode streamers develop. Note that for the low concentration, low ionization potential molecules, it takes the streamer 325 ns to reach $z = 1$ mm (Figure 4e) compared to the streamer created by the ionization of the high concentration, high potential molecules that travels $z = 1$ mm in only 100 ns (Figure 6e).

The results presented, which show streamer propagation modes result from the ionization of different families of molecules with unique concentration and ionization potentials, corroborates the qualitative model presented by Biller [11]. In Biller's hypothesis the specific charge generation mechanism involved in streamer development is not discussed, however researchers have theorized that the same mechanism drives both slow 2nd and fast 3rd mode streamers due to the similar streamer characteristics (*i.e.*, shape, light emission, etc.) of the two modes [4],[7]. Using plausible model parameter values, the results closely match experimental data suggesting that field ionization may be a possible key mechanism in driving both slow 2nd and fast 3rd mode filamentary positive streamers.

Due to the complex nature of liquids, a singular universal law that explains streamer formation in dielectric liquids does not exist. But the same is often true for the simplest phenomenon, such that a single law or mechanism that governs any physical event is often an oversimplification. Rather, laws are only obeyed within operating ranges, and as the conditions pass outside these ranges, then another law applies. The results in this paper suggest that the same concept holds for streamer development in transformer oil. For lower applied voltages (*i.e.*, $V_b \leq V_{app} \leq V_a$), streamers in transformer oil may result from field ionization of low concentration and low ionization potential oil molecules such as the trace aromatic hydrocarbons found in transformer oil. Alternatively, for higher applied voltages (*i.e.*, $V_{app} \geq V_a$), the results suggest that streamer development is from the field ionization of high concentration and high ionization potential oil molecules such as naphthenic or paraffinic hydrocarbons which constitute the bulk of the transformer oil volume. These characteristics of streamers due to low concentration and high concentration hydrocarbons are indicative of slow 2nd and fast 3rd mode streamers, respectively. The two streamer modes initiate at different applied voltages due to the unique ionization potentials of each hydrocarbon molecular species. For example, aromatic molecules generally have lower ionization potentials such that they ionize at lower applied voltages compared to naphthenic/paraffinic molecules that generally have higher ionization potentials and therefore need a greater applied voltage to ionize.

While it has been shown that field ionization is a possible dominant mechanism driving the development of positive filamentary streamers, it is by no means the only mechanism. There are many other factors that also affect the development of positive streamers. The model presented could be expanded to include other relevant mechanisms such as dissociation, vaporization, secondary cathode effects, impact ionization, etc., which would further result in more accurate results and better analysis. These new mechanisms will be examined in future continuing work.

References

- [1] A. Beroual, M. Zahn, A. Badent, K. Kist, A. J. Schwabe, H. Yamashita, K. Yamazawa, M. Danikas, W. D. Chadband, and Y. Torshin, "Propagation and structure of streamers in liquid dielectrics," *IEEE Electr. Insul. Mag.*, vol. 14, no. 2, pp. 6-17, Mar. 1998.
- [2] R. Tobazeon, "Prebreakdown phenomena in dielectric liquids," *IEEE Trans. Dielectr. Electr. Insul.*, vol. 1, no. 6, pp. 1132-1147, Dec. 1994.
- [3] R. E. Hebner. *Measurements of electrical breakdown in liquids*. Plenum Press, New York, pp. 519-537, 1988.
- [4] D. Linhjell, L. Lundgaard, and G. Berg, "Streamer propagation under impulse voltage in long point-plane oil gaps," *IEEE Trans. Electr. Insul.*, vol. 1, pp. 447-458, 1994.
- [5] Yu. V. Torshin, "On the existence of leader discharges in mineral oil," *IEEE Trans. Dielectr. Electr. Insul.*, vol. 2, no. 1, pp. 167-179, Feb. 1995.
- [6] L. Lundgaard, D. Linhjell, G. Berg, and S. Sigmond, "Propagation of positive and negative streamers in oil with and without pressboard interfaces," *IEEE Trans. Dielectr. Electr. Insul.*, vol. 5, no. 3, pp. 388-395, Jun. 1998.
- [7] O. Lesaint and G. Massala, "Positive streamer propagation in large oil gaps: experimental characterization of propagation modes," *IEEE Trans. Dielectr. Electr. Insul.*, vol. 5, no. 3, pp. 360-370, Jun. 1998.
- [8] Y. Nakao, T. Yamazaki, K. Miyagi, Y. Zakai, and H. Tagashira, "The effect of molecular structure on prebreakdown phenomena in dielectric liquids under nonuniform field," *Electrical Engineering in Japan*, vol. 139, no. 2, pp. 1-8, 2002.
- [9] J. C. Devins, S. J. Rzed, and R. J. Schwabe, "Breakdown and prebreakdown phenomena in liquids," *J. Appl. Phys.*, vol. 52, pp. 4531-4545, 1981.
- [10] L. Costeanu and O. Lesaint, "On mechanisms involved in the propagation of subsonic positive streamers in cyclohexane," in *Proc. IEEE 14th International Conference on Dielectric Liquids, ICDL 2002*, Graz, Austria, Jul. 7-12, 2002, pp. 143-146.
- [11] P. Biller, "A simple qualitative model for the different types of streamers in dielectric liquids," in *Proc. 12th International Conference on Conduction and Breakdown in Dielectric Liquids, ICDL 1996*, Baden-Dattwil, Switzerland, July 15-19, 1996, pp. 189-192.
- [12] M. Harada, Y. Ohga, I. Watanabe, and H. Watarai, "Ionization energies for solvated polycyclic aromatic hydrocarbons," *Chem. Phys. Lett.*, vol. 303, pp. 489-492, 1999.
- [13] H. S. Smalo, P.-O. Astrand, and S. Ingebrigtsen, "Calculation of ionization potentials and electron affinities for molecules relevant for streamer initiation and propagation," in *Proc. IEEE International Conference on Dielectric Liquids, ICDL 2008*, Futuroscope-Chasseneuil, France, Jun. 2008, pp. 1-4.
- [14] Nynas. Nynas Transformer Oil - Nytro 10XN (IEC 60296/03), 2008.
- [15] D. R. Lide, editor. *Physical Constants of Organic Compounds*. CRC Press/Taylor and Francis, Boca Raton, 89th edition, pp. 519-537, 2009.
- [16] F. O'Sullivan, Se-Hee Lee, M. Zahn, L. Pettersson, Rongsheng Liu, O. Hjortstam, T. Auletta, and U. Gafvert, "Modeling the effect of ionic dissociation on charge transport in transformer oil," in *Proc. IEEE Conference on Electrical Insulation and Dielectric Phenomena, CEIDP 2006*, Kansas City, MO, USA, Oct. 15-18, 2006, pp. 756-759.
- [17] N. J. Felici, "Blazing a fiery trail with the hounds," *IEEE Trans. Electr. Insul.*, vol. 23, no. 4, pp. 497-503, Aug. 1988.
- [18] M. Haidara and A. Denat, "Electron multiplication in liquid cyclohexane and propane," *IEEE Trans. Electr. Insul.*, vol. 26, no. 4, pp. 592-597, Aug. 1991.
- [19] W. G. Chadband, "On variations in the propagation of positive discharges between transformer oil and silicone fluids," *J. Phys. D: Appl. Phys.*, vol. 13, pp. 1299-1307, 1980.

- [20] F. M. O'Sullivan, "A model for the initiation and propagation of electrical streamers in transformer oil and transformer oil based nanofluids," PhD dissertation, Massachusetts Institute of Technology, Cambridge, MA, USA, 2007.
- [21] F. O'Sullivan, J. G. Hwang, M. Zahn, O. Hjortstam, L. Pettersson, Rongsheng Liu, and P. Biller, "A model for the initiation and propagation of positive streamers in transformer oil," in *Proc. IEEE 2008 Int. Symp. Electr. Insul., ISEI 2008*, Vancouver, BC, Canada, Jun. 2008, pp. 210-214.
- [22] J. G. Hwang, M. Zahn, L. A. A. Pettersson, O. Hjortstam, and Rongsheng Liu, "Modeling streamers in transformer oil: the transitional fast 3rd mode streamer," in *Proc. IEEE 9th Int. Conf. Prop. Appl. Dielectr. Mat., ICPADM 2009*, Harbin, China, Jul. 2009, pp. 573-578.
- [23] I. Adamczewski. Ionization, Conductivity and Breakdown in Dielectric Liquids. Taylor and Francis Ltd., London, 1969.
- [24] J. M. Meek and J. D. Craggs, editors. Electrical Breakdown of Gases. John Wiley & Sons, Chichester, 1978.
- [25] COMSOL AB, <http://www.comsol.com>.
- [26] Se-Hee Lee, Se-Yeon Lee, Young-Ki Chung, and Il-Han Park, "Finite-element analysis of corona discharge onset in air with artificial diffusion scheme and under Fowler-Nordheim electron emission," *IEEE Trans. Magn.*, vol. 43, no. 4, pp. 1453-1456, Apr. 2007.
- [27] G. E. Georgioui, R. Morrow, and A. C. Metaxas, "A two-dimensional finite element flux-corrected transport algorithm for the solution of gas discharge problems," *J. Phys. D: Appl. Phys.*, vol. 33, no. 19, pp. 2453-2466, 2000.
- [28] T. N. Tran, I. O. Golosnoy, P. L. Lewin, and G. E. Georgioui, "Two dimensional studies of Trichel pulses in air using the finite element method," in *Proc. Annual Report Conference on Electrical Insulation and Dielectric Phenomena, CEIDP 2009*, Virginia Beach, VA, USA, Oct. 2009.
- [29] CEI/IEC60897:1987. Methods for the determination of the lightning impulse breakdown voltage of insulating liquids. IEC, Geneva, Switzerland, 1987.
- [30] A. O. Allen. Drift Mobilities and Conduction Band Energies of Excess Electrons in Dielectric Liquids. NSRDS-NBS, 1976.
- [31] W. F. Schmidt, "Electronic conduction processes in dielectric liquids," *IEEE Trans. Electr. Insul.*, vol. EI-19, pp. 389-418, 1984.
- [32] M. Zahn. Electromagnetic Field Theory: A Problem Solving Approach. Robert E. Krieger Publishing Company, Inc., 2003.
- [33] J. G. Hwang, M. Zahn, F. M. O'Sullivan, L. A. A. Pettersson, O. Hjortstam, and R. Liu, "Effects of nanoparticle charging on streamer development in transformer oil- based nanofluids," *J. Appl. Phys.*, vol. 107, no. 1, pp. 014310-1 – 014310-17, Jan. 2010.
- [34] U. Gafvert, A. Jaksts, C. Tornkvist, and L. Walfridsson, "Electrical field distribution in transformer oil," *IEEE Trans. Electr. Insul.*, vol. 27, pp. 647-660, 1992.
- [35] W. F. Schmidt. Liquid State Electronics of Insulating Liquids. CRC Press, 1997.
- [36] Y. Nakamura, K. Shinsaka, and Y. Hatano, "Electron mobilities and electron-ion recombination rate constants in solid, liquid and gaseous methane," *J. Chem. Phys.*, vol. 78, pp. 5820-5824, 1983.
- [37] M. Tachiya, "Breakdown of the Debye theory of bulk ion recombination," *J. Chem. Phys.*, vol. 87, pp. 4108-4113, 1987.
- [38] J. Qian, R. P. Joshi, E. Schamiloglu, J. Gaudet, J. R. Woodworth, and J. Lehr, "Analysis of polarity effects in the electrical breakdown of liquids," *J. Phys. D: Appl. Phys.*, vol. 39, pp. 359-369, 2006.
- [39] T. J. Lewis, "Basic electrical processes in dielectric liquids," *IEEE Trans. Dielectr. Electr. Insul.*, vol. 1, no. 4, pp. 630-643, Aug. 1994.
- [40] M. Sack, Y. Julliard, R. Badent, and A. J. Schwab, "Electrical trees in solids and streamers in liquids - structural analogies and differences," in *Proc. Annual Report Conference on Electrical Insulation and Dielectric Phenomena, CEIDP 2002*, Cancun, Mexico, Oct. 20-24, 2002, pp. 60-63.
- [41] Sir J. Townsend. The Theory of Ionization of Gases by Collision. Constable & Company, London, 1910.
- [42] R. Badent, "Streamer model based on electronic processes in liquids," in *Proc. Annual Report Conference on Electrical Insulation and Dielectric Phenomena, CEIDP 1999*, vol. 2, Austin, TX, USA, Oct. 17-20, 1999, pp. 447-450.
- [43] W. G. Chadband, "Electrical breakdown - from liquid to amorphous solids," *J. Phys. D.: Appl. Phys.*, vol. 24, pp. 56-64, 1991.
- [44] T. J. Lewis, "A new model for the primary process of electrical breakdown in liquids," *IEEE Trans. Dielectr. Electr. Insul.*, vol. 5, no. 3, pp. 306-315, Jun. 1998.

- [45] C. Zener, "A theory of the electrical breakdown of solid dielectrics," *Proc. Roy. Soc. A*, vol. 145, pp. 523-529, 1934.
- [46] J. G. Hwang. Elucidating the mechanisms behind pre-breakdown phenomena in transformer oil systems. PhD dissertation, Massachusetts Institute of Technology, Cambridge, MA, USA, 2010.
- [47] S. Sakamoto and H. Yamada, "Optical study of conduction and breakdown in dielectric liquids," *IEEE Trans. Electr. Insul.*, vol. EI-15, pp. 171-181, 1980.
- [48] W. G. Chadband, "The ubiquitous positive streamer," *IEEE Trans. Electr. Insul.*, vol. 23, no. 4, pp. 697-706, Aug. 1988.
- [49] B. Halpern and R. Gomer, "Field ionization in liquids," *J. Chem. Phys.*, vol. 51, pp. 1048-1056, 1969.
- [50] W. Schnabel and W. F. Schmidt, "Polymerization by high electric fields: field emission and field ionization," *J. Polymer Sci.*, vol. 42, pp. 273-280, 1973.
- [51] W. An, K. Baumung, and H. Bluhm, "Underwater streamer propagation analyzed measurements from pressure release," *J. Appl. Phys.*, vol. 101, no. 5, 2007.
- [52] A. Beroual and R. Tobazeon, "Prebreakdown phenomena in liquid dielectrics," *IEEE Trans. Electr. Insul.*, vol. EI-21, no. 4, pp. 613-627, Aug. 1986.
- [53] R. A. Holroyd and W. F. Schmidt, "Transport of electrons in nonpolar fluids," *Annu. Rev. Phys. Chem.*, vol. 40, pp. 439-468, 1989.
- [54] J. K. Baird, "Negative ion photodetachment and the electron effective mass in liquids," *J. Chem. Phys.*, vol. 79, pp. 316-320, 1983.
- [55] O. Lesaint and M. Jung, "On the relationship between streamer branching and propagation in liquids: influence of pyrene in cyclohexane," *J. Phys. D: Appl. Phys.*, vol. 33, pp. 1360-1368, 2000.
- [56] S. Ingebrigtsen, L. E. Lundgaard, and P.-O. Astrand, "Effects of additives on prebreakdown phenomena in liquid cyclohexane: I. streamer initiation," *J. Phys. D: Appl. Phys.*, vol. 40, pp. 5624-5634, 2007.
- [57] M. Zahn. Space charge dynamics of liquids. PhD dissertation, Massachusetts Institute of Technology, Cambridge, MA, USA, 1970.
- [58] M. Zahn and J. R. Melcher, "Space-charge dynamics of liquids," *Phys. Fluids*, vol. 15, no. 7, pp. 1197-1206, July 1972. Erratum, *Phys. Fluids*, vol. 15, no. 11, pp. 2082, 1972.
- [59] M. Zahn, "Space charge coupled interfacial waves," *Phys. Fluids*, vol. 17, no. 2, pp. 343-352, 1974.
- [60] Rongsheng Liu, C. Tornkvist, Y. Chandramouli, O. Girlanda, and L. A. A. Pettersson, "Ester fluids as alternative for mineral oil: the difference in streamer velocity and LI breakdown voltages," in *Proc. Annual Report Conference on Electrical Insulation and Dielectric Phenomena, CEIDP 2009*, Virginia Beach, VA, USA, Oct. 2009.

2. Effects of Nanoparticle Charging on Streamer Development on Streamer Development in Transformer Oil-Based Nanofluids

Sponsors

This work was supported by ABB Corporate Research, Vasteras, Sweden via the MIT Energy Initiative and the National Science and Engineering Research Council of Canada.

Project Staff

George Hwang, Jouya Jadidian, and Markus Zahn

Introduction

The widespread use of transformer oil for high voltage insulation and power apparatus cooling has led to extensive research work aimed at enhancing both its dielectric and thermal characteristics. A particularly innovative example of such work is the development of dielectric nanofluids (NFs). These materials are manufactured by adding nanoparticle suspensions to transformer oil, with the aim of enhancing some of the oil's insulating and thermal characteristics. Researchers have investigated transformer oil-based NFs using magnetite nanoparticles from ferrofluids [1]-[7]. The research showed that a transformer oil-based magnetic NF could be used to enhance the cooling of a power transformer's core.

Electrical breakdown testing of magnetite NF found that for positive streamers the breakdown voltage of the NFs was almost twice that of the base oils during lightning impulse tests [2]. The lightning impulse withstand results obtained by Segal *et al.* [1]-[5] of increased transformer oil breakdown strength with the addition of conducting nanoparticles for two common transformer oils (i.e., Univolt 60 and Nytro 10X) and their associated NFs are summarized in Table I. Also, the propagation velocity of positive streamers was reduced by the presence of nanoparticles, by as much as 46% for Univolt-colloid nanofluid. The results are significant because a slower streamer requires more time to traverse the gap between electrodes to cause breakdown. This allows more time for the applied impulse voltage to be extinguished. These results are very important in that it indicates that the presence of the magnetite nanoparticles in the oil samples inhibits the processes, which leads to electrical breakdown. The results found by Segal *et al.* are in direct conflict with conventional wisdom and experience regarding the breakdown of dielectric liquids, where the presence of conducting particulate matter in a dielectric liquid is expected to decrease the breakdown strength.

A comprehensive electrodynamic analysis of the processes that take place in electrically stressed transformer oil-based nanofluids is presented. The results demonstrate that conductive nanoparticles act as electron scavengers in electrically stressed transformer oil-based NFs, converting fast electrons to slow negatively charged nanoparticles [8]-[11]. Due to the low mobility of these nanoparticles, the development of a net space charge zone at the streamer tip is hindered, suppressing the propagating electric field wave that is needed to drive electric field dependent molecular ionization and ultimately streamer propagation further into the liquid. A general expression for the charging dynamics of a nanoparticle in transformer oil with finite conductivity is derived to show that the trapping of fast electrons onto slow nanoparticles is the cause of the decrease in the positive streamer velocity. This explains the paradoxical fact that NFs manufactured from conductive nanoparticles have superior positive electrical breakdown performance to that of pure oil.

Experimental evidence for transformer oil showed that positive streamers emanating from the positive electrode tend to initiate at lower applied voltages and propagate faster and further than negative streamers [2],[12],[13]. As a result, positive streamers constitute a greater risk to oil insulated high voltage electrical equipment than do negative streamers and are the focus of this work.

Table I: Results of impulse voltage withstand testing in 25.4 mm electrode gap system [2].

Fluid	Breakdown voltage (kV)		Time-to-breakdown (μ s)		Avg. streamer velocity (km/s)	
	Positive	Negative	Positive	Negative	Positive	Negative
Univolt 60 oil	86	170	12	27	2.12	0.94
Univolt nanofluid	157	154	26	15	0.98	1.69
Nytro 10X oil	88	177	16	23	1.59	1.10

Charge Relaxation Time

To understand why a transformer oil-based NF exhibits differing electrical breakdown characteristics to that of pure oil, it is necessary to understand how the presence of the nanoparticles in the oil modifies the fundamental electrodynamic processes. The charge relaxation time constant of the nanoparticle material has a major bearing on the extent to which the electrodynamic processes in the liquid are modified. If the nanoparticles' charge relaxation time constant is short relative to the time scales of interest for streamer growth, their presence in the oil will significantly modify the electrostatics. If, on the other hand, the nanoparticles' relaxation time constant is long relative to the time scales of interest for streamer growth, their presence will have little effect on the electrostatics.

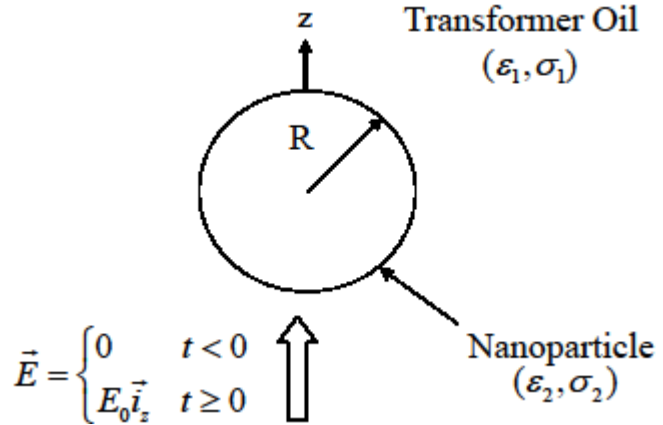


Figure 1: Nanoparticle of an arbitrary material with a radius R , permittivity ϵ_2 and conductivity σ_2 , surrounded by transformer oil with a permittivity of ϵ_1 and conductivity σ_1 stressed by a uniform z -directed electric field turned on at $t=0$.

In order to calculate a general expression for the relaxation time constant of a nanoparticle of arbitrary material in the transformer oil consider Fig. 1. The spherical nanoparticle of an arbitrary material has radius R , permittivity ϵ_2 , and conductivity σ_2 and is surrounded by transformer oil with conductivity of $\sigma_1 = 1 \times 10^{-12}$ S/m and permittivity of $\epsilon_1 = 2.2\epsilon_0$, where $\epsilon_0 = 8.854 \times 10^{-12}$ F/m is the permittivity of free space. At time $t=0^+$, a z -directed electric field $\vec{E} = E_0 \vec{i}_z$ is switched on at $r \rightarrow \infty$. The presence of the nanoparticle causes the electric field distribution in the oil near the nanoparticle to deviate from the applied z -directed field. The electric field distribution in the oil is calculated by using the separation of variables method to solve Laplace's equation for the electric potential V (i.e., $\nabla^2 V = 0$, $\vec{E} = -\nabla V$) where a negligible space charge density is assumed. The time dependent radial and polar components of the electric field in the oil outside the nanoparticle are [8],[14],[15]

$$E_{r0}(r, \theta) = E_0 \left[1 + \frac{2R^3}{r^3} Y_c \exp\left(-\frac{t}{\tau_r}\right) + \frac{2R^3}{r^3} \Sigma_c \left(1 - \exp\left(-\frac{t}{\tau_r}\right) \right) \right] \cos \theta \quad (1)$$

$$E_{\theta 0}(r, \theta) = E_0 \left[-1 + \frac{R^3}{r^3} Y_c \exp\left(-\frac{t}{\tau_r}\right) + \frac{R^3}{r^3} \Sigma_c \left(1 - \exp\left(-\frac{t}{\tau_r}\right) \right) \right] \sin \theta \quad (2)$$

where the charge relaxation time constant τ_r for the transformer oil/nanoparticle system is

$$\tau_r = \frac{2\epsilon_1 + \epsilon_2}{2\sigma_1 + \sigma_2} \quad (3)$$

and

$$Y_c = \frac{\epsilon_2 - \epsilon_1}{2\epsilon_1 + \epsilon_2}, \quad (4)$$

$$\Sigma_c = \frac{\sigma_2 - \sigma_1}{2\sigma_1 + \sigma_2}. \quad (5)$$

Consider now the magnetite Fe_3O_4 NF studied by researchers in Refs. [1]–[7] where $\sigma_2 = 1 \times 10^4$ S/m at room temperature [16] and $\delta_2 \approx 80 \text{ \AA}$ [17]. The relaxation time constant of the magnetite in transformer oil is $\tau_{r, (\text{Fe}_3\text{O}_4)} = 7.47 \times 10^{-14}$ s. As this shows, the relaxation time constant for magnetite nanoparticles in transformer oil is extremely short. Relative to the nanosecond to microsecond timescales involved in streamer propagation, this small relaxation time constant is essentially instantaneous so that the addition of magnetite nanoparticles to the transformer oil will dramatically affect the electrodynamics during streamer development. The relaxation time constant is analogous to the time constant of an RC circuit that describes the charging rate of a capacitor (nanoparticle) when the source (free electrons at $r \rightarrow \infty$) is turned on at $t=0$. Therefore, the small relaxation time constant for magnetite nanoparticles effectively means that the surface charging due to the injected electrons can be considered to be instantaneous. Furthermore, for a NF manufactured using magnetite, the extremely short relaxation time constant means that the electric field lines tend to converge upon the relaxed nanoparticles as if they were perfect conductors.

As a comparison to the NF manufactured with magnetite nanoparticles, other common nanoparticles, such as ZnO and Al_2O_3 , have relaxation time constants of $\tau_{r, (\text{ZnO})} = 1.05 \times 10^{-11}$ s and $\tau_{r, (\text{Al}_2\text{O}_3)} = 42.2$ s. Note that due to Al_2O_3 's low conductivity, its relaxation time constant is very long. Therefore, there would be negligible surface charging of Al_2O_3 nanoparticles in the time scales of interest for which streamer development occurs.

Modeling the Charge Dynamics of a Perfectly Conducting Nanoparticle

To model the electrodynamics within an electrically stressed transformer oil-based nanofluid it is first necessary to model the charging of the nanoparticles in oil. This model parallels the Whipple-Chalmers model used for the modeling of rain drop charging in thunderstorms taking the flow velocity of oil to be zero [14],[15],[19]. Consider the situation shown in Fig. 2 for a perfectly conducting nanoparticle (i.e., $\sigma_2 \rightarrow \infty$). A uniform z-directed electric field $E_0 \hat{z}$ is switched on at $t=0$, and a uniform electron charge density ρ_e with electron mobility μ_e is injected into the system from $z \rightarrow \infty$. The injected electrons travel along the electric field lines and approach the nanoparticle where the radial electric field is positive, $0 < \theta < \pi/2$, as shown in Fig. 2. The electric field lines will terminate on the bottom side with a negative surface charge and emanate from the top side with a positive surface charge on the particle as shown in Figs. 2a, 2b, and 2c. The electrons in the transformer oil near a nanoparticle will move opposite to the direction of the field lines and become deposited on the nanoparticle where the surface charge is positive. The rate at which a nanoparticle captures electrons is strongly dependent upon its charge relaxation time constant such that nanoparticles with a short relaxation time constant quickly capture free electrons.

The charging dynamics for a perfectly conducting nanoparticle ($\sigma_2 \rightarrow \infty$) is examined first. Afterwards, the analysis is generalized to finitely conducting nanoparticles to model nanoparticles manufactured from real materials.

At $t=0^+$, a nanoparticle with infinite conductivity is perfectly polarized and the radial electric field is initially positive everywhere on the upper hemisphere defined by $\theta=0$ to $\pi/2$ as shown in Fig. 2 corresponding to positive surface charge density $\sigma_s = \epsilon_0 E_r(r=R, \theta) > 0$. Therefore, the electrons can be initially deposited on the nanoparticle at all points on the upper hemispherical surface. Once the electrons deposit on the nanoparticle they redistribute themselves uniformly on the equipotential surface, so that the total negative charge on the nanoparticle increases from zero with time. This charging process modifies the electric field outside the nanoparticle and continually reduces the area of the nanoparticle surface that has a positive radial electric field component (the charging window on the particle surface) as shown in Figs. 2b and 2c until a point is reached when no portion of the particle's surface has a positive radial electric field component as shown in Fig. 2d. In this situation the nanoparticle is said to be charge saturated as no additional negative charge can flow onto the sphere.

The solution for the electric field outside the perfectly conducting (i.e., $\sigma_2 \rightarrow \infty, \Sigma_c = 1, \tau_r = 0$) spherical nanoparticle is the superposition of the solutions of Eqs. (1) and (2) plus the radial field component caused by the already deposited electrons with net charge $Q(t)$ where $Q(t) \leq 0$.

$$\vec{E} = \left[E_0 \left(1 + \frac{2R^3}{r^3} \right) \cos \theta + \frac{Q(t)}{4\pi\epsilon_0 r^2} \right] \vec{i}_r - E_0 \left[1 - \frac{R^3}{r^3} \right] \sin \theta \vec{i}_\theta \quad r > R \quad (6)$$

Electrons can only be deposited on the nanoparticle where the radial component of the electric field on the nanoparticle surface is positive (i.e., $E_r(r=R) \geq 0$). This gives a window for electron charging over a range of angles determined by

$$\cos \theta \geq -\frac{Q(t)}{12\pi\epsilon_0 E_0 R^2} \quad (7)$$

Since the magnitude of $\cos \theta$ cannot be greater than one, the electron saturation charge for the nanoparticle is

$$Q_s = -12\pi\epsilon_0 R^2 E_0 \quad (8)$$

When the nanoparticle charges to this saturation value the radial component of the electric field at every point on the particle's surface will be negative and so no more electrons can be deposited on the particle. The critical angle θ_c , where the radial component of the electric field at $r=R$ is zero, is defined as when Eq. (7) is an equality

$$\cos \theta_c = Q(t) / Q_s \quad (9)$$

Representative values in transformer oil of mobilities and charge densities of positive and negative ions and electrons are $\mu_p \approx \mu_n \approx 1 \times 10^{-9} \text{ m}^2 \text{ V}^{-1} \text{ s}^{-1}$, $\mu_e \approx 1 \times 10^{-4} \text{ m}^2 \text{ V}^{-1} \text{ s}^{-1}$ and $\rho_p \approx -\rho_n \approx 1000 \text{ C/m}^3$ and $\rho_e \approx -1000 \text{ C/m}^3$. The effective conductivities of ions are then $\sigma_{p,n} = \rho_p \mu_p = -\rho_n \mu_n \approx 1 \times 10^{-6} \text{ S/m}$ while electrons have a much higher effective ohmic conductivity of $\sigma_e = -\rho_e \mu_e \approx 1 \times 10^{-1} \text{ S/m}$. With the much lower transformer oil ohmic conductivity of $\sigma_1 \approx 1 \times 10^{-12} \text{ S/m}$, the dominant charge carriers that charge the nanoparticles are the electrons so that the nanoparticle charging current for angles $0 < \theta < \theta_c$ is

$$J_r(r=R, \theta) = -\rho_e \mu_e E_r(r=R, \theta) = -3\rho_e \mu_e E_0 \left[\cos \theta - \frac{Q(t)}{Q_s} \right] \quad (10)$$

where $\rho_e < 0$ and $\mu_e > 0$. The total nanoparticle charging current is

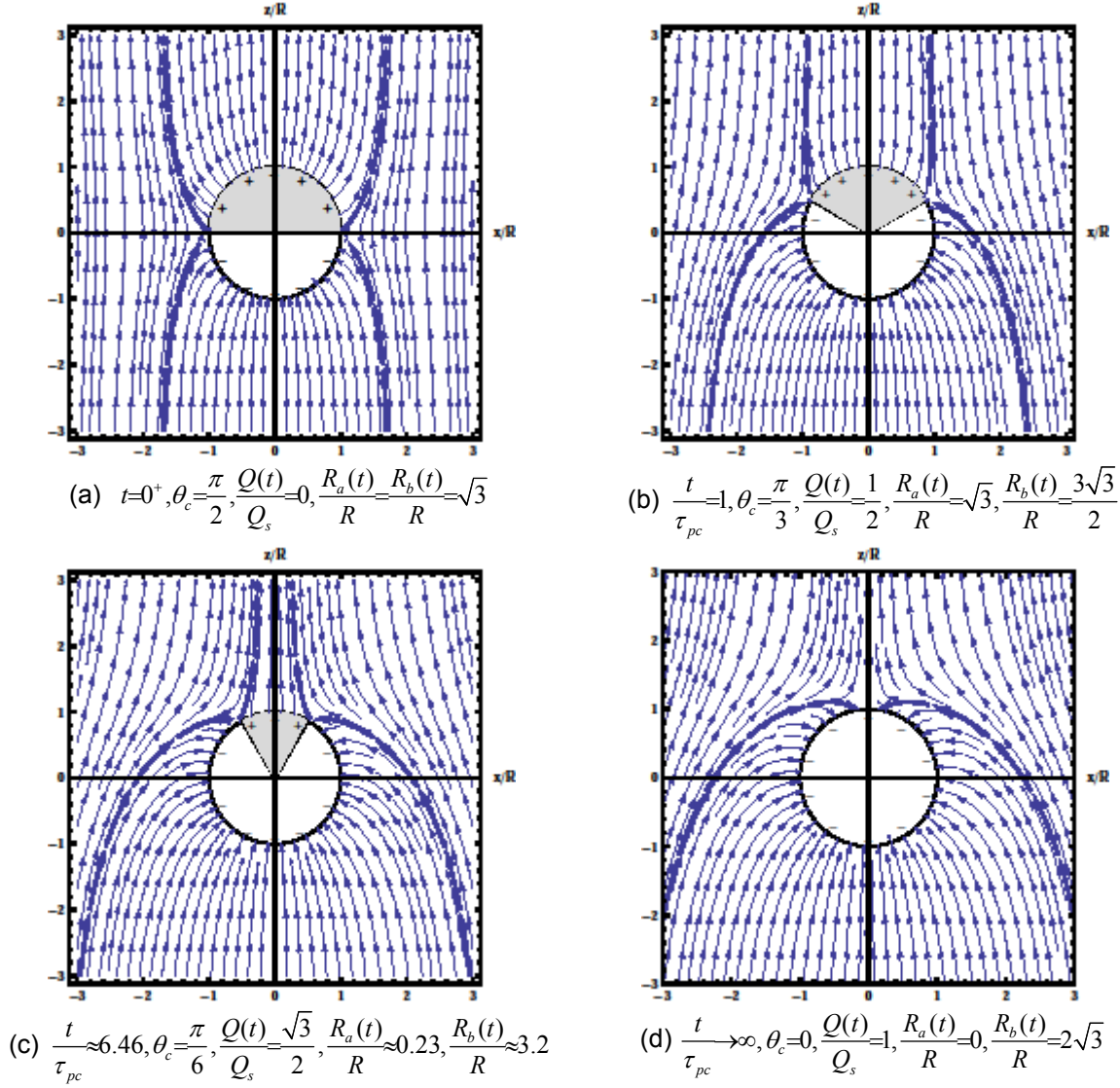


Figure 2: Electric field lines for various times after a uniform z-directed electric field is turned on at $t = 0$ around a perfectly conducting spherical nanoparticle of radius R surrounded by transformer oil with permittivity ϵ_1 , conductivity σ_1 , and free electrons with uniform charge density ρ_e and mobility μ_e . The thick electric field lines terminate on the particle at $r = R$ and $\theta = \theta_c$ where $E_r(r = R) = 0$ and separate field lines that terminate on the nanoparticle from field lines that go around the particle. The cylindrical radius $R_a(t)$ of Eq. (21) of the separation field line at $z \rightarrow +\infty$ defines the charging current $I(t)$ in Eq.(23). The cylindrical radius $R_b(t)$ of Eq. (22) defines the separation field line at $z \rightarrow -\infty$. The dominant charge carrier in charging the nanoparticles are electrons because of their much higher mobilities than positive and negative ions. The conductivity of transformer oil, $\sigma_1 \approx 1 \times 10^{-12}$ S/m, is much less than the effective conductivity of the electrons, $\sigma_e \approx -\rho_e \mu_e \approx 1 \times 10^{-1}$ S/m. The electrons charge each nanoparticle to saturation, $Q_s = -12\pi\epsilon_1 E_0 R^2$ as given in Eq. (8) with time constant $\tau_{pc} = 4\epsilon_1 / (|\rho_e| \mu_e)$ given in Eq. (12). The electric field lines in this figure were plotted using Mathematica StreamPlot [18].

$$\frac{dQ(t)}{dt} = -\int_{\theta=0}^{\theta_c} J_r 2\pi R^2 \sin \theta d\theta = \frac{Q_s}{\tau_{pc}} \left[1 - \frac{Q(t)}{Q_s} \right]^2 \quad (11)$$

where the time constant for nanoparticle charging τ_{pc} is

$$\tau_{pc} = \frac{4\dot{q}}{|\rho_e| \mu_e} \quad (12)$$

The charging dynamics of the perfectly conducting nanoparticle can be found by time integrating the nanoparticle charging current equation given by Eq. (11). Therefore, the charge on a perfectly conductive nanoparticle by electron scavenging is

$$Q(t) = \frac{Q_s \frac{t}{\tau_{pc}}}{1 + \frac{t}{\tau_{pc}}} \quad (13)$$

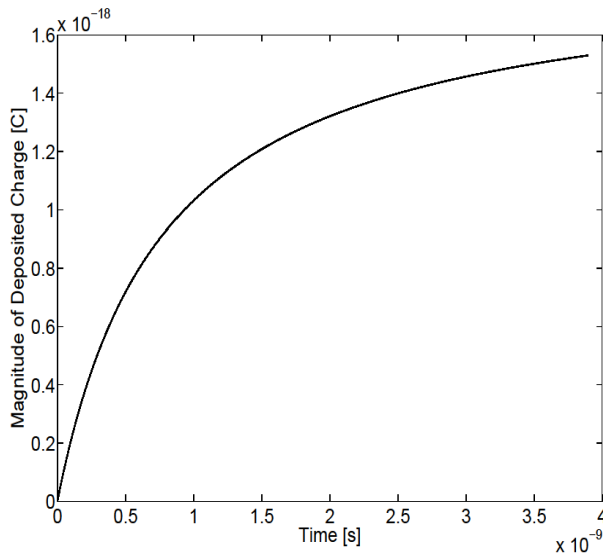


Figure 3: Charging dynamics, $|Q(t)|$, of a perfectly conducting nanoparticle versus time in transformer oil as given by Eq. (13) with $Q_s = -1.836 \times 10^{-18}$ C (~ 11 electrons) and $\tau_{pc} = 7.79 \times 10^{-10}$ s.

where the initial condition is $Q(t=0)=0$.

For the purposes of evaluating the values of Q_s and τ_{pc} , the following additional parameter values are used: $e = 1.6 \times 10^{-19}$ C, $E_0 = 1 \times 10^8$ V/m,

$\dot{q} = 2.2\dot{q}_0$ and $R = 5 \times 10^{-9}$ m. These values are reasonable estimates for the parameter values at the tip of a streamer in a transformer oil-based nanofluid [9]. The values for Q_s and τ_{pc}

found by using these parameters are -1.836×10^{-18} C (~ 11 electrons) and 7.79×10^{-10} s, respectively. The charging dynamics plotted in Fig. 3 illustrate that the perfectly conducting nanoparticle initially captures charge rapidly; however, as time increases the particle charging rate decreases until the particle's charge saturates at Q_s . These features are due to the reduction in the charge capture window. As the particle captures electrons the repulsion increases between the negatively charged nanoparticles and the mobile free electrons in the surrounding oil.

Free charge carriers in the nanofluid will tend to move along the electric field lines that converge on the relaxed nanoparticle, depositing negative charge on the top surface and positive charge on the bottom surface of the particle in Fig. 2. Because electron mobility is much higher than positive ion mobility, the nanoparticles trap electrons at a much faster rate than positive ions, meaning that the nanoparticles effectively become slow negative ions. The mobility of such a charged spherical particle in transformer oil is given by Eq. (14) [15], where the viscosity of transformer oil is approximately $\eta = 0.02$ Pa s.

$$\mu_{np} = \frac{|Q_s|}{6\pi\eta R} = 9.7 \times 10^{-10} \text{ m}^2 \text{V}^{-1} \text{s}^{-1} . \quad (14)$$

Electric Field Lines

Analysis is also facilitated through the use of a vector potential \vec{A} for the electric field, given in (1) and (2), when the electric field due to the space charge density is small compared to the electric field due to the applied voltage such that $\nabla \cdot \vec{E} \approx 0$. Then with no dependence on the angle ϕ , the vector potential $\vec{A} = A_\phi(r, \theta) \vec{i}_\phi$ and the electric field are related as

$$\vec{E}(r, \theta) = \nabla \times \vec{A}(r, \theta) = \frac{1}{r \sin \theta} \frac{\partial}{\partial \theta} (\sin \theta A_\phi) \vec{i}_r - \frac{1}{r} \frac{\partial}{\partial r} (r A_\phi) \vec{i}_\theta . \quad (15)$$

The vector potential is

$$A_\phi(r, \theta) = \frac{E_0 r \sin \theta}{2} \left[1 + \frac{2R^3}{r^3} Y_c \exp\left(-\frac{t}{\tau_r}\right) + \frac{2R^3}{r^3} \Sigma_c \left(1 - \exp\left(-\frac{t}{\tau_r}\right) \right) \right] - \frac{Q(t) \cos \theta}{4\pi\epsilon_0 r \sin \theta} . \quad (16)$$

Electric field lines are everywhere tangent to the electric field and related to the vector potential in Eq.(15) as

$$\frac{dr}{rd\theta} = \frac{E_r}{E_\theta} = \frac{\frac{1}{r \sin \theta} \frac{\partial}{\partial \theta} (\sin \theta A_\phi)}{-\frac{1}{r} \frac{\partial}{\partial r} (r A_\phi)} . \quad (17)$$

After cross multiplication and reduction, the electric field lines are lines of constant $r \sin \theta A_\phi(r, \theta)$ because

$$d(r \sin \theta A_\phi(r, \theta)) = \frac{\partial}{\partial r} (r \sin \theta A_\phi) dr + \frac{\partial}{\partial \theta} (r \sin \theta A_\phi) d\theta = 0 \quad (18)$$

where the constant for a given electric field line is found by specifying one (r, θ) value of a point that the field line goes through.

A perfectly conducting nanoparticle has $\tau_r = 0$ so that $e^{-t/\tau_r} = 0$, $\Sigma_c = 1$, and $A(t) = 3$. The field lines are obtained from Eq. (16) as

$$\Lambda_1(r, \theta) = r \sin \theta A_\phi(r, \theta) = \frac{E_0 r^2 \sin^2 \theta}{2} \left[1 + \frac{2R^3}{r^3} \right] - \frac{Q(t) \cos \theta}{4\pi\epsilon_0} = \text{constant} . \quad (19)$$

The separation field line that demarcates the region where electrons charge a nanoparticle is shown by the thicker field line in Fig. 2 and terminates on the nanoparticle at $r=R$, $\theta=\theta_c$. This field line obeys the equation

$$\Lambda_1(r=R, \theta=\theta_c) = \frac{3E_0 R^2 \sin^2 \theta_c}{2} - \frac{Q(t) \cos \theta_c}{4\pi\epsilon_0} = \frac{3E_0 R^2}{2} \left[1 + \left(\frac{Q(t)}{Q_s} \right)^2 \right] . \quad (20)$$

Evaluating Eq. (19) at $r \rightarrow \infty$, $\theta \rightarrow 0$ and equating it to Eq. (20) gives the cylindrical radius $R_a(t)$ of the electron charging demarcation field line of the upper hemisphere. The cylindrical radius is

$$R_a(t) = \lim_{r \rightarrow \infty, \theta \rightarrow 0} (r \sin \theta) = \sqrt{3} R \left[1 - \frac{Q(t)}{Q_s} \right] = \frac{\sqrt{3} R}{1 + \frac{t}{\tau_{pc}}} \quad (21)$$

where Eq. (13) is used and $R_a(t)$ decreases with time as the particle charges up.

Similarly, there is a separation field line that passes through $(r=R, \theta=\theta_c)$ but terminates in the lower region at $r \rightarrow \infty$, $\theta \rightarrow \pi$ with cylindrical radius

$$R_b(t) = \lim_{r \rightarrow \infty, \theta \rightarrow \pi} (r \sin \theta) = \sqrt{3}R \left[1 + \frac{Q(t)}{Q_s} \right] = \sqrt{3}R \frac{2t + \tau_{pc}}{t + \tau_{pc}} \quad (22)$$

which separates field lines that terminate on the spherical nanoparticle for $\theta_c < \theta < \pi$ from field lines that go around the nanoparticle. The combined separation field line that passes through $(r=R, \theta=\theta_c)$ and $r \rightarrow \infty$ and $\theta=0$ or π are drawn as thicker lines in Fig. 2.

The total current at $r \rightarrow \infty$ passing through the area $\pi R_a^2(t)$ is the total current incident onto the nanoparticle

$$I(t) = \rho_e \mu_e E_0 \pi R_a^2(t) = \frac{Q_s}{\tau_{pc}} \left[1 - \frac{Q(t)}{Q_s} \right]^2 \quad (23)$$

which matches the right-hand side of Eq. (11).

References

- [1] V. Segal and K. Raj, Ind. J. Eng. Mater. Sci. **5**, 416, 1998.
- [2] V. Segal, A. Hjorstberg, A. Rabinovich, D. Nattrass, and K. Raj, IEEE International Symposium on Electrical Insulation (ISEI'98), 1998, pp. 619–622.
- [3] V. Segal, A. Rabinovich, D. Nattrass, K. Raj, and A. Nunes, J. Magn. Magn. Mater. **215-216**, 513 2000.
- [4] V. Segal, D. Nattrass, K. Raj, and D. Leonard, J. Magn. Magn. Mater. **201**, 70, 1999.
- [5] V. Segal, US Patent No. 5,863,455, 26 January 1999.
- [6] K. Raj and R. Moskowitz, US Patent No. 5,462,685, 31 October 1995.
- [7] T. Cader, S. Bernstein, and S. Crowe, US Patent No. 5,898,353, 27 April 1999.
- [8] F. M. O'Sullivan, Ph.D. thesis, Massachusetts Institute of Technology, 2007.
- [9] F. O'Sullivan, J. G. Hwang, M. Zahn, O. Hjortstam, L. Pettersson, R. Liu, and P. Biller, IEEE International Symposium on Electrical Insulation (ISEI'08), 2008, pp. 210–214.
- [10] J. G. Hwang, M. Zahn, F. O'Sullivan, L. A. A. Pettersson, O. Hjortstam, and R. Liu, 2009 Electrostatics Joint Conference, 2009.
- [11] COMSOL URL <http://www.comsol.com>.
- [12] A. Beroual, M. Zahn, A. Badent, K. Kist, A. J. Schwabe, H. Yamashita, K. Yamazawa, M. Danikas, W. G. Chadband, and Y. Torshin, IEEE Electr. Insul. Mag. USA **14**, 6 1998.
- [13] R. E. Hebner, *Measurements of Electrical Breakdown in Liquids*: Plenum, New York, 1988, pp. 519–537.
- [14] M. Zahn, *Electromagnetic Field Theory: A Problem Solving Approach*: Robert E. Krieger, Malabar, Florida, 2003.
- [15] J. R. Melcher, *Continuum Electromechanics*: MIT Press, Cambridge, Massachusetts, 1981.
- [16] J. M. D. Coey, A. E. Berkowitz, L. I. Balcells, F. F. Putris, and F. T. Parker, Appl. Phys. Lett. **72**, 734 1998.
- [17] A. Dey, A. De, and S. K. De, J. Phys.: Condens. Matter **17**, 5895 2005.
- [18] MATHEMATICA URL <http://reference.wolfram.com/mathematica/ref/StreamPlot.html>.
- [19] F. J. W. Whipple and J. A. Chalmers, Q. J. R. Meteorol. Soc. **70**, 103, 1944.
- [20] S. Wolfram, *The Mathematica Book*, 4th ed. Wolfram Media, /Cambridge

3. Charge Transport Mechanisms in Liquid-Solid Insulation Systems

Sponsors

This work was supported by ABB Corporate Research, Vasteras, Sweden via the MIT Energy Initiative.

Project Staff

Jouya Jadidian, George Hwang, and Markus Zahn

Introduction

Power transformers, transmission cables, and other high voltage equipment often utilize composite insulation systems. These insulators usually comprise both liquid and solid insulating materials. Liquid-solid systems such as transformer oil-pressboard systems constitute the major composite insulation system that is used to improve the insulation capability of power transformers. Experimental evidence has shown that streamer pre-breakdown phenomena in liquid-solid insulation systems often differ from liquid-only systems [1]. Such phenomena in composite insulation systems are characterized by charge transport between the two distinct liquid and solid dielectrics [2].

A one-dimensional transient analysis of unipolar charge injection and transport between two planar electrodes stressed by an applied step voltage was first presented in [3]. The model consisted of solving charge migration equations between electrodes in a single region. This work extends the closed-form results of [3] to a two-phase (liquid and solid) insulation system in a series planar geometry. The time and space solutions for electric field, charge density, and terminal voltage for a current source are solved in the transient-state for various charge injection constitutive laws by using the method of characteristics which converts the governing partial differential equations in time and space into a set of ordinary differential equations in the time frame of the moving charge. From this analysis the surface charge density at the liquid/solid interface is found as a function of time.

In the previous studies [2, 3], the analysis has been confined to space-charge-limited injection, whereby the electric field at the charge injecting electrode is zero while the charge density is infinite keeping the injection current finite. In the present work, we have generalized this injection boundary condition such that the electric field at the emitter electrode can be non-zero. A step current source is considered for a time dependent case study. The liquid dielectric is assumed to have unipolar ion conduction described by a constant mobility while the solid dielectric is modeled by an Ohmic conduction model. The results give charge density and electric field distributions as a function of time and space, charge trajectories in the liquid region as well as terminal voltage and surface charge density at the liquid/solid interface as a function of time. Most of the analysis yields closed-form expressions which are in reasonable agreement with numerical simulations [2, 4, 5].

Governing Equations

A one-dimensional migration-Ohmic model where all quantities only depend on coordinate x and time t , describes charge transport phenomena in the two region series liquid-solid geometry shown in Fig. 1. Region I represents a transformer oil region with positive charge mobility μ and dielectric permittivity ϵ_I while Region II represents a pressboard region with Ohmic conductivity σ and dielectric permittivity ϵ_{II} . It is assumed that only the positive electrode at $x=0$ injects positive electric charge into the system. These charges travel from the first region and pass through the interface into Region II with surface charge remaining on the interfacial surface at $x=a$. In this model, we have selected representative values in Table 1 for transformer oil and pressboard as Regions I and II respectively (Fig. 1). Steady-state and transient analyses yield closed-form expressions of the electric field, volume and surface densities and voltage drop across the regions for a step current source. Gauss' law and conservation of charge are:

$$\nabla \cdot \vec{E} = \rho / \epsilon \quad (1)$$

$$\nabla \cdot \vec{J} + \frac{\partial \rho}{\partial t} = 0 \quad (2)$$

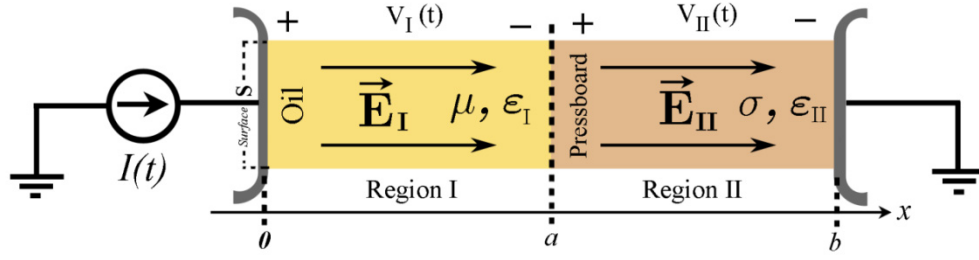


Figure 1: Two series dielectric planar model excited by a time dependent current source, where Region I is described by a carrier mobility μ and permittivity ϵ_I representing transformer oil and Region II is described by Ohmic conductivity σ and permittivity ϵ_{II} representing pressboard.

Table 1: Representative values for parameters of liquid and solid dielectrics

Parameter	Symbol	Value
Permittivity of Liquid Region (Region I)	ϵ_I	$2 \times 10^{-11} \text{ Fm}^{-1}$
Permittivity of Solid Region (Region II)	ϵ_{II}	$4 \times 10^{-11} \text{ Fm}^{-1}$
Positive Ion Mobility in Liquid Region (Region I)	μ	$10^{-9} \text{ m}^2 \text{ V}^{-1} \text{ s}^{-1}$
Conductivity of Solid Region (Region II)	σ	$3 \times 10^{-12} \text{ } \Omega^{-1} \text{ m}^{-1}$
Applied Current Density (Current Source Condition)	$J_0 = I_0/S$	10^{-7} Am^{-2}
Liquid Region (I) Thickness	a	0.0125 m
Total Thickness (Liquid Region (I) and Solid Region (II))	b	0.025 m

One-dimensional Analysis

Equations (1) and (2) can be written for the one-dimensional (x -direction) system in Region I as:

$$\frac{\partial E_I(x,t)}{\partial x} = \rho / \epsilon_I \quad (3)$$

$$\frac{\partial J_I(x,t)}{\partial x} + \frac{\partial \rho(x,t)}{\partial t} = 0 \Rightarrow J_I(x,t) + \epsilon_I \frac{\partial E_I(x,t)}{\partial t} = \frac{I(t)}{S} \quad (4)$$

The boundary conditions for the electric field, surface charge density $\sigma_s(t)$, and the current density at the interfacial surface are:

$$\epsilon_{II} E_{II}(x=a_+,t) - \epsilon_I E_I(x=a_-,t) = \sigma_s(t) \quad (5)$$

$$J_{II}(x=a_+,t) - J_I(x=a_-,t) + \frac{\partial \sigma_s(t)}{\partial t} = 0 \quad (6)$$

Since the electric field in both regions is conservative ($\nabla \times \vec{E} = 0$) in both regions, the voltage drop across the electrodes is:

$$V(t) = V_I(t) + V_{II}(t) = \int_0^a E_I dx + \int_a^b E_{II} dx. \quad (7)$$

In Region I, the positive charge carriers are injected at the positive electrode ($x=0$) assuming a linear injection law. According to this law, the injected volume charge density at the positive electrode is given by a product of electric field at $x=0$ and a constant injection coefficient A :

$$\rho(x=0,t) = AE_I(x=0,t). \quad (8)$$

According to Eq. (4) and Eq. (8), the current density in Region I is:

$$J_I = \mu \rho(x=0,t)E_I(x=0,t) + \varepsilon_I \frac{\partial E_I(x=0,t)}{\partial t} = \mu A[E_I(x=0,t)]^2 + \varepsilon_I \frac{\partial E_I(x=0,t)}{\partial t} \quad (9)$$

As a special case of space charge limited injection, A is assumed to be infinitely large. In order to keep the current density J_0 finite when $A \rightarrow \infty$, the electric field at $x=0$ must be zero (i.e., $E_I(x=0,t)=0$). In each region, the total current density is related to the electric field as:

$$J_I = \rho \mu E_I + \varepsilon_I \frac{\partial E_I}{\partial t}, \quad J_{II} = \sigma E_{II} + \varepsilon_{II} \frac{\partial E_{II}}{\partial t}. \quad (10)$$

Steady State Solutions ($\partial/\partial t=0$)

The trapped surface charge on the interfacial surface between the two regions can be obtained from Gauss' law:

$$\sigma_s = \varepsilon_{II} E_{II} - \varepsilon_I E_I \quad (11)$$

For steady state conditions, the surface charge density on the interface is constant; the current density in both regions is also constant for $0 < x < b$:

$$J_{II} - J_I = 0 \rightarrow J_I = J_{II} = J_0 \quad (12)$$

Hence, from Gauss' law in the steady state and Eq. (3):

$$J_0 = J_I = \rho \mu E_I = \mu \varepsilon_I E_I \frac{dE_I}{dx} = J_{II} = \sigma E_{II} \Rightarrow J_0 = \frac{d}{dx} \left(\frac{1}{2} \varepsilon_I \mu E_I^2 \right) = \sigma E_{II}. \quad (13)$$

By solving Eq. (13), the electric field in each region is:

$$E_I = \sqrt{2(J_0 x + C) / (\varepsilon_I \mu)}, \quad E_{II} = J_0 / \sigma \quad (14)$$

The constant, C is calculated from the steady state boundary condition at the positive electrode (linear charge injection law, Eq. (8)). Since the steady state current density is independent of x , we have:

$$J_0 = \mu \rho E_I(x=0) = \mu A[E_I(x=0)]^2 = \frac{2AC}{\varepsilon_I} \Rightarrow C = \frac{\varepsilon_I J_0}{2A} \Rightarrow E_I = \sqrt{\frac{J_0}{\mu} \left(\frac{2x}{\varepsilon_I} + \frac{1}{A} \right)} \quad (15)$$

To evaluate the voltage as a function of current density, we integrate the electric field in both regions (Eq. (7)) which yields:

$$V = \frac{2}{3} \sqrt{\frac{2J_0}{\varepsilon_I \mu}} \left[\left(a + \frac{\varepsilon_I}{2A} \right)^{3/2} - \left(\frac{\varepsilon_I}{2A} \right)^{3/2} \right] + \frac{J_0}{\sigma} (b - a) \quad (16)$$

By solving Eq. (16) for the square root of J_0 , the current density can be found as a function of applied voltage, charge injection coefficient and dielectric parameters:

$$J_0 = \left[\frac{\sigma}{6(b-a)\sqrt{\varepsilon_I \mu}} \left(\left(\frac{\varepsilon_I}{A} \right)^{3/2} - \left(2a + \frac{\varepsilon_I}{A} \right)^{3/2} + \left(\left(\frac{\varepsilon_I}{A} \right)^{3/2} - \left(2a + \frac{\varepsilon_I}{A} \right)^{3/2} \right)^2 + 36 \frac{\varepsilon_I \mu}{\sigma} (b-a) V_0 \right)^{1/2} \right]^2 \quad (17)$$

Mathematically there are two roots for the square root term of J_0 in Eq. (16), however, since E_I which is proportional to the square root of J_0 according to Eq. (14) must be positive, the only applicable result for square root of J_0 is the positive definite solution which results in Eq. (17). Since the steady state current density does not depend on x , $J=J_I=J_{II}=J_0$ remains constant for $0 < x < b$. Figure 2 plots the steady state current density J_0 in terms of the linear injection coefficient A for different values of constant applied voltage. The total current density in Eq. (17) significantly depends on A only if its magnitude is of order $Aa/\varepsilon_I \sim 1$. When A goes to infinity (so that $Aa/\varepsilon_I \gg 1$), the current density for the space charge limited condition is:

$$J_0 = \left[\frac{\sigma}{3(b-a)\sqrt{\varepsilon_I \mu}} \left(-\sqrt{2a^3} + \sqrt{2a^3 + 9 \frac{\varepsilon_I \mu}{\sigma} (b-a) V_0} \right) \right]^2 \quad (18)$$

From Eq. (14), the steady state charge density in the liquid region (Region I) is found using Gauss' law:

$$\rho(x) = \varepsilon_I \frac{dE_I}{dx} = \sqrt{\frac{J_0}{\mu \left(\frac{2x}{\varepsilon_I} + \frac{1}{A} \right)}} \quad (19)$$

whereas the surface charge density σ_s on the interfacial surface at $x=a$ is found from Eq. (11):

$$\sigma_s = \frac{\varepsilon_{II} J_0}{\sigma} - \sqrt{\frac{J_0}{\mu} \left(2a\varepsilon_I + \frac{\varepsilon_I^2}{A} \right)} \quad (20)$$

For the space charge limited condition ($A \rightarrow \infty$), the space charge density in Region I is:

$$\rho(x) = \varepsilon_I \frac{dE_I}{dx} = \sqrt{\frac{J_0 \varepsilon_I}{2\mu x}}, \quad \sigma_s = \frac{\varepsilon_{II} J_0}{\sigma} - \sqrt{\frac{2\varepsilon_I J_0 a}{\mu}} \quad (21)$$

Equations (19) and (21) agree with the results of [2].

Transient Solutions

The transient analysis of unipolar charge transport in a migration-Ohmic system has a time varying current source (Fig. 1) resulting in both conduction and displacement current in the two region series dielectrics of Fig. 1. We particularly assume that the terminal current $I(t) = J_0 S u(t)$ is a step function at $t=0$ being $I(t=0_-) = 0$ and $I(t \geq 0_+) = J_0 S$ where S is the electrode area. We assume an initially unexcited system with a linear charge injection law (Eq. (8)) at $x=0$. From Eqs (10), the current density in Regions I and II has both conduction and displacement currents:

$$J = J_0 = J_I = \rho \mu E_I(x,t) + \varepsilon_I \frac{\partial E_I(x,t)}{\partial t} = J_{II} = \sigma E_{II}(t) + \varepsilon_{II} \frac{\partial E_{II}(t)}{\partial t} \quad (22)$$

where E_{II} only depends on time and not position.

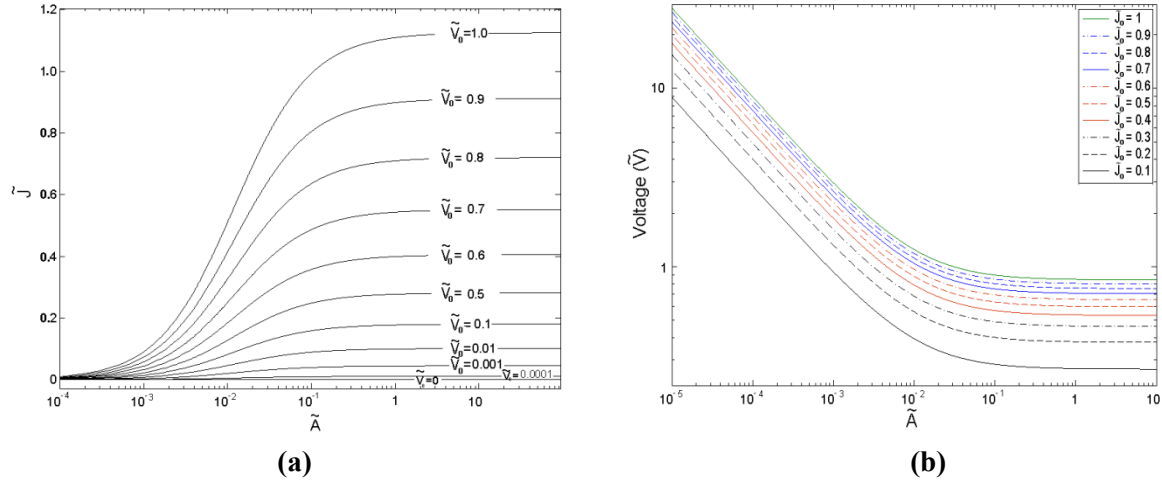


Figure 2: Theoretical plots of (a): steady state non-dimensional current density $\tilde{J} = J(a^3 / (\epsilon_I \mu V_0^2))$ for various applied non-dimensionalized DC voltages $\tilde{V} = V / V_0$ and (b): non-dimensionalized DC voltage $\tilde{V} = V \sqrt{\epsilon_I \mu / (J_0 a^3)}$ for various non-dimensional current densities $\tilde{J} = J / J_0$ as a function of non-dimensionalized charge injection coefficient $\tilde{A} = Aa / \epsilon_I$.

Determining Electric Field in Region I

Using the method of characteristics for Region I, we define the total derivative of electric field in the reference frame of the moving charge:

$$\frac{dE_I}{dt} = \frac{\partial E_I}{\partial t} + \frac{dx}{dt} \cdot \frac{\partial E_I}{\partial x} = \frac{J_0}{\epsilon_I} \quad \text{on} \quad \frac{dx}{dt} = \mu E_I \quad (23)$$

which has a general solution for the electric field as:

$$E_I(x, t) = \frac{J_0}{\epsilon_I} (t - t_0) + E_I(x_0, t_0) \quad (24)$$

and a general solution for charge trajectory position as:

$$x(t) = \frac{J_0 \mu}{2 \epsilon_I} (t - t_0)^2 + E_I(x_0, t_0) (t - t_0) + x_0 \quad (25)$$

where $x_0 = x(t = t_0)$. Using Eqs. (3), (4), and (9) the charge density in the reference frame of the moving charge obeys the equations:

$$\underbrace{\frac{\partial \rho}{\partial t} + \mu E_I \frac{\partial \rho}{\partial x}}_{=d\rho/dt} + \frac{\mu}{\epsilon_I} \rho^2 = 0 \quad \Rightarrow \quad \frac{d\rho}{dt} + \frac{\mu \rho^2}{\epsilon_I} = 0 \quad \text{on} \quad \frac{dx}{dt} = \mu E_I \quad (26)$$

By solving the ordinary differential equations in Eq. (26), the volume charge density in Region I is:

$$\rho(t) = \frac{\rho(t_0)}{1 + \frac{\mu}{\varepsilon_I} \rho(t_0) (t - t_0)} \quad \text{on } \frac{dx}{dt} = \mu E_I \quad (27)$$

Figure 3 shows the time-space domain of the transient one-dimensional model of charge transport in the migration-Ohmic regions. As can be seen in Fig. 3, injected charge travels on trajectories (solid black curves in Region I) until it reaches the interfacial surface at $x=a$. Initial charge density $\rho(t_0)$ in Eq. (27) is the charge density at the starting point of a charge trajectory. At Sub-region I₁ (the area which is labeled as “initial condition problem” in Fig. 3), the charge density is zero since for our problem it has been assumed that $\rho(x, t=0)=0$. With an initial zero charge density, the charge density given by Eq. (27) remains zero on its entire trajectory. In Sub-region I₁, electric field $E_I(t)$ is merely a function of time and not position. The positive charge density (given by Eq. (27)) is injected from the positive electrode (which makes $\rho(x=0, t=t_0)$ non-zero) in Sub-region I₂ of Fig. 3, labeled as “Charge injection problem”. It should be noted that, the electric field at the positive electrode $E_I(x, t=0)$ itself varies with time.

The demarcation curve in Fig. 3 is an important charge trajectory which separates Sub-region I₁ (Initial condition problem) from the Sub-region I₂ (Charge injection problem). The electric field on the demarcation curve is the same as trajectories of Sub-region I₁, since $\rho(x=0, t=0)=0$. Thus for demarcation curve $x_d(t)$ and other charge trajectories in Sub-region I₁, the electric field is obtained from Eq. (24) with $E_I(x_0, t_0=0)=0$. The electric field at $t=0$ is zero since no charge is yet injected into Region I. The demarcation curve is characterized by Eq. (25) with $x_0=0, t_0=0$ and $E_I(x_0=0, t_0=0)=0$. The demarcation time (charge time of flight) is defined as the time t_d at which $x_d(t=t_d)=a$ (with $t_0=0$):

$$t_d = \sqrt{\frac{2\varepsilon_I a}{\mu J_0}} \quad (28)$$

To the right of the demarcation curve $x_d(t)$, we have charge trajectories emanating from $(x_0=0, t_0)$. To obtain the electric field in Region I at any arbitrary point in the time-space domain such as (x_i, t_i) in Fig. 3, we need first to determine $E_I(x=0, t=t_0)$ to serve as an initial condition. With the charge injection boundary condition of (8), the governing equation for the electric field at the charge injection electrode at $x=0$ is:

$$A\mu E_I^2(x=0, t) + \varepsilon_I \frac{dE_I(x=0, t)}{dt} = J_0 \quad (29)$$

with solution:

$$E_I(x=0, t) = \sqrt{\frac{J_0}{\mu A}} \tanh\left(\sqrt{\mu A J_0} \frac{t}{\varepsilon_I}\right). \quad (30)$$

The result of Eq. (30) satisfies the initial condition of zero field at $t=0$ and also agrees with the steady-state electric field in Region I (Eq. (15)) where $x=0$:

$$E_I(x=0, t=0)=0, \quad E_I(x=0, t \rightarrow \infty)=\sqrt{\frac{J_0}{\mu A}} \quad (31)$$

Knowing the electric field at the positive charge injection electrode for all values of t_0 , $E_I(x=0, t_0)$, we are able to determine the electric field for any point in Region I in time and space as given from Eqs. (24) and (30) for $x_0=0$. Also, we can obtain the charge trajectories of unipolar charge emanating from the $x=0$ electrode at $t=t_0$ from Eqs. (25) and (30) with $x_0=0$. The equations for electric field and charge trajectories are not complete since t_0 or equivalently $\Delta t=t-t_0$ is not known for arbitrary values of time t and space x in Region I. According to Eq. (25), by solving the quadratic equation for Δt , we have two solutions. Because Δt should always be positive, the correct solution is:

$$\Delta t = (t - t_0) = -\frac{\epsilon_I}{J_0} \left[E_I(x=0, t_0) - \sqrt{E_I^2(x=0, t_0) + \frac{2J_0}{\mu \epsilon_I} x(t)} \right] \quad (32)$$

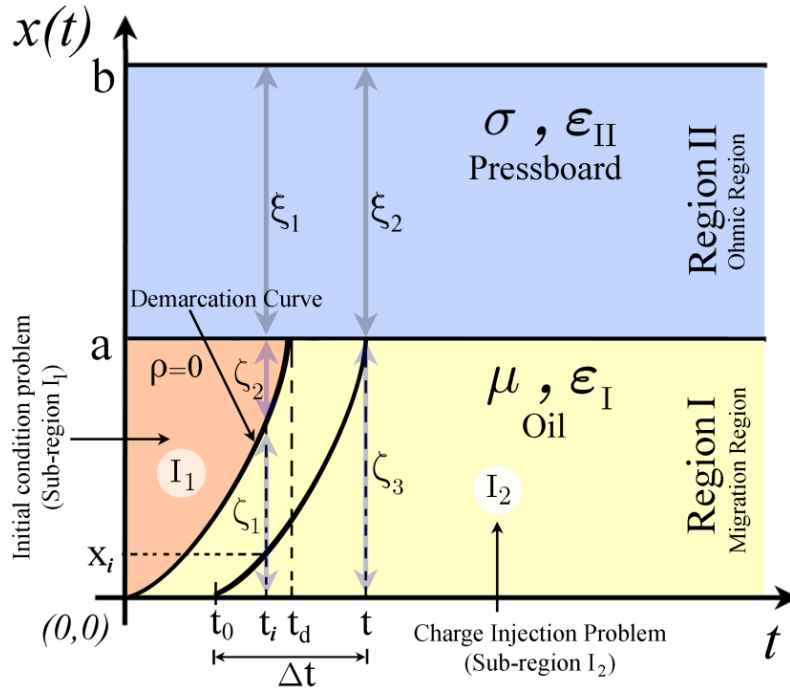


Figure 3: Time-space domain for the transient one-dimensional model of charge transport in the migration-Ohmic system. In the migration region, the demarcation curve starting at $x=0, t=0$, separates the initial condition problem (Sub-region I_1) from the charge injection problem (Sub-region I_2). The integration paths (ζ_1 and ζ_2 in Region I and ξ_1 in Region II) are labeled for times less than the charge time of flight (t_d) starting at $x=0, t=0$ and ending at $x=a, t=t_d$ and (ζ_3 in Region I and ξ_2 in Region II) greater than t_d . These integration paths are necessary for determination of the voltage across the layers.

To determine the voltage across the regions we need to integrate the electric field over the space x in both regions according to Eq. (7). To evaluate electric field at any arbitrary (x_i, t_i) in Region I, $E_I(x=0, t_0)$ is required. To obtain $E_I(x=0, t_0)$, initial time t_0 should be derived for any x_i and t_i from Eq. (32) which is a non-linear equation. Since, no algebraic solution is available for t_0 and $\Delta t = t - t_0$ (Fig. 3) in terms of any arbitrary point x_i and t_i , it is not possible to determine E_I at any point in the time-space

domain. Nonetheless, according to the first part of Eq. (10) and by deriving the electric field at $x = a$ and $x = 0$ we are still able to find the voltage across the Region I (liquid region):

$$\varepsilon_I \frac{\partial E_I}{\partial t} + \mu \rho E_I = \varepsilon_I \frac{\partial E_I}{\partial t} + \mu \varepsilon_I E_I \frac{\partial E_I}{\partial x} = \varepsilon_I \frac{\partial E_I}{\partial t} + \frac{\partial}{\partial x} \left(\frac{1}{2} \mu \varepsilon_I E_I^2 \right) = J_0 \quad (33)$$

By integrating x from x_1 to x_2 at fixed time in Eq. (33), we have:

$$\int_{x=x_1}^{x_2} \left[\frac{\partial E_I}{\partial t} + \frac{\partial}{\partial x} \left(\frac{1}{2} \mu \varepsilon_I E_I^2 \right) \right] dx = \int_{x=x_1}^{x_2} \frac{J_0}{\varepsilon_I} dx \quad (34)$$

which reduces to:

$$\frac{dV_I}{dt} + \frac{1}{2} \mu \left(E_I^2(x=x_2, t) - E_I^2(x=x_1, t) \right) = \frac{J_0(x_2 - x_1)}{\varepsilon_I} \quad (35)$$

For $t < t_d$, x_1 and x_2 in Eq. (35) should include integration path ζ_1 in Sub-region I_2 (Fig. 3). The electric field which is required for integration path ζ_2 in Sub-region I_1 is already known as Eq. (24) for $x_0 = 0$. Thus, Eq. (40) for $t < t_d$ results in:

$$\frac{dV_I}{dt} = \frac{J_0 a}{\varepsilon} - \frac{1}{2} \mu \left(\left(\frac{J_0}{\varepsilon_I} t \right)^2 - \frac{J_0}{\mu A} \tanh^2 \left(\sqrt{\mu A J_0} \frac{t}{\varepsilon_I} \right) \right) \quad (36)$$

For $t > t_d$, the integration path ζ_3 is entirely in Sub-region I_2 (Fig. 3). Thus, the voltage drop across the Region I for $t > t_d$ can be found by assuming, $x_1 = 0$ and $x_2 = a$ in Eq. (35):

$$\frac{dV_I}{dt} = \frac{J_0 a}{\varepsilon} - \frac{1}{2} \mu \left(\left(\frac{J_0}{\varepsilon_I} (t - t_0) + \sqrt{\frac{J_0}{\mu A}} \tanh \left(\sqrt{\mu A J_0} \frac{t_0}{\varepsilon_I} \right) \right)^2 - \frac{J_0}{\mu A} \tanh^2 \left(\sqrt{\mu A J_0} \frac{t}{\varepsilon_I} \right) \right) \quad (37)$$

According to Eqs. (36) and (37), we merely need the electric field at $x = a$ and $x = 0$ for any time to calculate V_I in Sub-region I_2 . In other words, we need t_0 or equivalently Δt to find the voltage drop across Region I. To solve the nonlinear equation in Eq. (32) for Δt , we must use numerical approaches. Distinct solutions of Δt by the Gauss-Newton algorithm and the Levenberg-Marquardt algorithm result in essentially the same results.

Determining Electric Field in Region II

Determination of the electric field in Region II is more straightforward by solving:

$$\varepsilon_{II} \frac{\partial E_{II}}{\partial t} + \sigma E_{II} = J_0 \quad (38)$$

Thus, we already have E_{II} at any time which is not a function of space x :

$$E_{II} = \frac{J}{\sigma} (1 - e^{-t/\tau}), \quad \text{where} \quad \tau = \frac{\varepsilon_{II}}{\sigma} \quad (39)$$

By integrating V_I in Eqs. (36) and (37) we have the voltage drop across the Region I for any time. Also from Eq. (44), V_{II} is found by integrating the electric field over space in Region II. By adding the voltage drops in both regions:

$$V = \begin{cases} \frac{J_0 a}{\varepsilon_I} t - \frac{\mu J_0^2}{6 \varepsilon_I^2} t^3 + \frac{J_0}{2A} t - \frac{\varepsilon_I}{2A} \sqrt{\frac{J_0}{\mu A}} \tanh\left(\sqrt{\mu A J_0} \frac{t}{\varepsilon_I}\right) + \frac{J_0(b-a)}{\sigma} (1 - e^{-t/\tau}) & 0 \leq t < t_d \\ J_0(t-t_0) \left[\frac{a}{\varepsilon_I} - \frac{1}{2A} \tanh^2\left(\sqrt{\mu A J_0} \frac{t_0}{\varepsilon_I}\right) \right] - \frac{\mu J_0^2}{6 \varepsilon_I^2} (t-t_0)^3 - \frac{J_0}{\varepsilon_I} \sqrt{\frac{\mu J_0}{A}} \tanh\left(\sqrt{\mu A J_0} \frac{t_0}{\varepsilon_I}\right) \frac{(t-t_0)^2}{2} \\ + \frac{J_0}{2A} (t-t_0) - \frac{\varepsilon_I}{2A} \sqrt{\frac{J_0}{\mu A}} \left[\tanh\left(\sqrt{\mu A J_0} \frac{t}{\varepsilon_I}\right) - \tanh\left(\sqrt{\mu A J_0} \frac{t_0}{\varepsilon_I}\right) \right] + \frac{J_0(b-a)}{\sigma} (1 - e^{-t/\tau}) & t \geq t_d \end{cases} \quad (40)$$

For the space charge limited injection, according to Eq. (32) when $A \rightarrow \infty$, then $\Delta t = t - t_0 \rightarrow t_d$. Therefore, the space charge limited solution for voltage V is:

$$V = \begin{cases} \frac{J_0 a}{\varepsilon_I} t - \frac{\mu J_0^2}{6 \varepsilon_I^2} t^3 + \frac{J_0(b-a)}{\sigma} (1 - e^{-t/\tau}) & 0 \leq t < t_d \\ \frac{J_0 a}{\varepsilon_I} t_d - \frac{\mu J_0^2}{6 \varepsilon_I^2} t_d^3 + \frac{J_0(b-a)}{\sigma} (1 - e^{-t/\tau}) & t \geq t_d \end{cases} \quad (41)$$

Where $V(t)$ is continuous at t_d . Figure 5 shows the time variations of voltage across both layers for different values of linear injection coefficient A . As can be seen in this figure, for A greater than 10^{-8} , the response of the systems is very similar to the response of the system with A infinite.

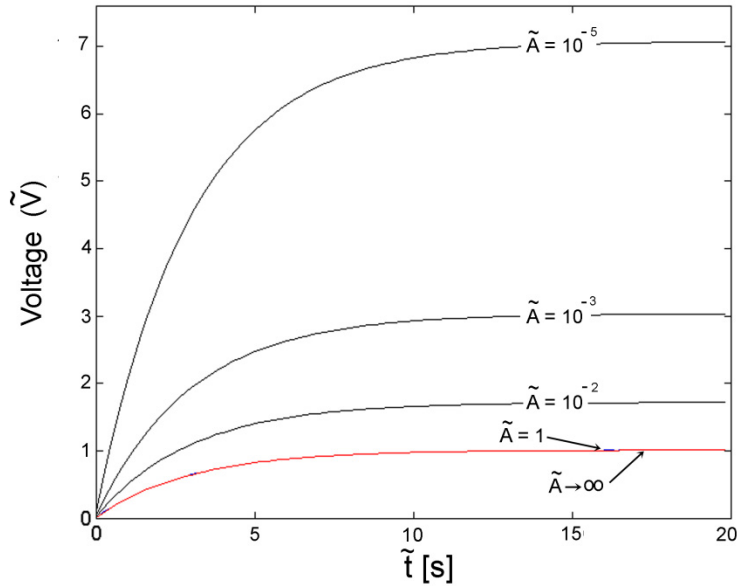


Figure 4: Non-dimensionalized time dependent voltage $\tilde{V} = V \sqrt{\varepsilon_I \mu / (J_0 a^3)}$ for a step current across the migration-Ohmnic layers for different values of non-dimensionalized charge injection coefficient ($\tilde{A} = Aa / \varepsilon_I$).

References

- [1] L. Lundgaard, D. Linhjell, G. Berg, and S. Sigmond, "Propagation of positive and negative streamers in oil with and without pressboard interfaces," *IEEE Trans. Dielectr. Electr. Insul.*, vol. 5, no. 3, pp. 388-395, June 1998.
- [2] J. G. Hwang, "Elucidating the mechanisms behind pre-breakdown phenomena in transformer oil systems," Ph.D. dissertation, Massachusetts Institute of Technology, Cambridge, MA, USA, June 2010.
- [3] M. Zahn, C. F. Tsang and S. C. Pao, "Transient electric field and space-charge behavior for unipolar ion conduction" *J. Appl. Phys.*, vol. 45, pp. 2432 -2440, 1974.
- [4] F. O'Sullivan, "A model for the initiation and propagation of electrical streamers in transformer oil and transformer oil based nanofluids," Ph.D. dissertation, Massachusetts Institute of Technology, Cambridge, MA, USA, June 2007.
- [5] J. G. Hwang, M. Zahn, F. O'Sullivan, L. A. A. Pettersson, O. Hjortstam, and R. Liu, "Effects of nanoparticle charging on streamer development in transformer oil-based nanofluids", *J. of Appl. Phys.*, vol. 107, pp. 014310-014310-17, 2010.

4. Dielectric Materials for Advanced Applications

Sponsors

This work was supported by Siemens Corporate Research, Inc.

Project Staff

Xuewei Zhang, Qing Yang, and Markus Zahn.

Introduction

Charge injection from high-voltage stressed electrodes depends on the dielectric and electrode materials, impurity contents and electrode surface treatment. Electric field distributions, distorted by space charge, cannot then be simply calculated from knowledge of the electrode configuration, dielectric properties and source excitation.

To help understand space charge effects, typically due to charge injection from electrodes and charge dissociation in the dielectric, we consider the simplest case of planar electrodes with an x directed electric field E_x which is distorted by net charge density $\rho(x)$ only dependent on the x coordinate. In such a one dimensional electrode geometry, Gauss's law requires that the slope of the electric field distribution be proportional to the local charge density:

$$\nabla \cdot \mathbf{E} = \frac{\partial E_x}{\partial x} = \frac{\rho}{\varepsilon} \quad (1)$$

where ε is the material dielectric permittivity.

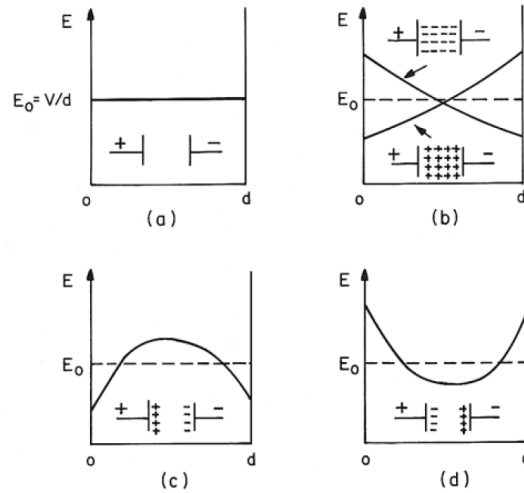


Figure 1. Space charge distortion of the electric field distribution between parallel plate electrodes with spacing d at voltage V so that the average electric field is $E_0 = V/d$. (a) uniform field with no charge injection; (b) unipolar positive or negative charge injection; (c) bipolar homocharge injection with field depressed at both electrodes; and (d) bipolar heterocharge injection with field enhanced at both electrodes.

For the case of no volume charge shown in Figure 1(a), the electric field is uniform given by $E_0 = V/d$ for a voltage V across a gap d . In Figure 1(b), unipolar injection of positive (or negative) charge has the electric field reduced at the anode (or cathode) but enhanced at the cathode (or anode), thus possibly leading to electrical breakdown at lower voltages. For bipolar homocharge injection in Figure 1(c), positive charge is injected at the anode and negative charge is injected at the cathode, so that the electric field is lowered at both electrodes and is largest in the central region. Since electrical breakdown often initiates at the electrode-dielectric interface, this case can allow higher voltage operation without breakdown. If the voltage suddenly reverses, the electric field must also instantaneously reverse, but the charge distribution cannot immediately change because it takes some time for the volume charge to migrate. Thus, for early times after voltage reversal, positive charge is near the cathode and negative charge is near the anode, increasing the fields near both electrodes as shown in Figure 1(d). Such a bipolar heterocharge

configuration leads to breakdown at lower voltages as has been found in HVDC polyethylene cables when the voltage is instantaneously reversed to reverse the direction of power flow.

Past work [1] has shown that using water between a positive stainless steel electrode and a negative aluminum electrode resulted in homopolar charge injection from both electrodes that increased the electric breakdown strength in water by 40% over the opposite voltage polarity with no charge injection. Thus an intensive theoretical and experimental program is in progress for increasing the electrical breakdown strength of dielectric materials and electrode structures for use in advanced electric power systems, biomedical technologies, and other high voltage applications. As the first part of this research, an intensive and thorough literature review was conducted on the current state of knowledge on the causes of electrical breakdown and on known methods for increasing the electrical breakdown strength in vacuum, gaseous, liquid, and solid dielectrics.

We study the smart use of space charge injection by choosing optimum metal/dielectric material combinations to increase electric breakdown strength. For electric field mapping measurements of high-voltage stressed transparent dielectrics, our approach is based on the Kerr electro-optic effect [2]. High voltage stressed liquids are usually birefringent, in which case the refractive indices for light (of free-space wavelength λ) polarized parallel, n_{\parallel} , and perpendicular, n_{\perp} , to the local electric field are related by $n_{\parallel} - n_{\perp} = \lambda B E^2$, where B is the Kerr constant and E is the magnitude of the applied electric field. In a parallel-plate electrode configuration, we assume the magnitude and direction of E to be constant along the light path. Thus the phase shift $\Delta\phi$ between light-field components polarized parallel and perpendicular to the applied electric field and propagating in the direction perpendicular to the plane of the applied electric field along an electrode length L is $\Delta\phi = 2\pi B L E^2$. The modulation effect of the electric field can be detected by comparing the intensities of incident light and transmitted light. This data is collected by a modern computerized CCD camera. In this report, we will present the measurement results in the gap filled with the high Kerr constant propylene carbonate under dc and pulsed high voltages.

Summary of Literature Search

The literature search is divided into four parts: A) vacuum, B) gaseous, C) liquid and D) solid dielectrics. Over 300 publications have been reviewed. However, in this report, we will only present a very brief summary and list only the most important references. Special attention is paid to some counter-intuitive experimental facts which may be of practical interest.

A) Vacuum

The breakdown voltage of a vacuum gap is influenced by four categories of factors: (1) residual gas: pressure and material content; (2) electrodes: temperature, material, surface condition, contaminations; (3) gap: size and shape; (4) external conditions: applied voltage, circuit resistance, extraneous particles, environmental and operational factors. To improve the electrical strength, we usually make adjustments with respect to one or more of these factors. The insulation design can optimize the contour of the gap geometry; the breakdown strength may be higher at a different pressure or temperature; the various conditionings, coatings and electrode surface treatments can remove adhering particles and gases and can smooth the electrode surface; the avoidance of hostile external conditions can also ensure a better insulation performance.

The residual gas pressure should be as low as possible to prevent electrical breakdown due to collisional ionization. However, an anomaly is observed for effect of pressure on the breakdown strength in a stainless steel sphere-plane gap of 20 cm [3]. With the increase in pressure from 10^{-5} Torr to about 4×10^{-4} Torr, the breakdown voltage doubles. Further increase in pressure will sharply reduce the breakdown strength. Hence, there seems to be an optimum pressure in this case. Another interesting aspect is the "state" of the electrode: bulk solid or just a thin-film? Generally speaking, the breakdown strength of the thin-film electrode gap is much smaller than that of a smooth surface solid electrode gap under identical conditions. However, it was reported in [4], that when thin-film anodes which could be penetrated by incident electrons were used in the field emission microscope, a 20% increase in the breakdown voltage could be produced. The electrode configuration consists of a hemispherical stainless steel cathode with a radius of curvature of the working surface of 12 mm, an anode made from metal foil and a Faraday cup to collect electrons coming from the anode.

B) Gaseous

Air is the most commonly used gaseous insulation medium in high voltage power networks because it is free, abundant and self-restoring after a breakdown. The electrical breakdown behavior of air gaps has been thoroughly investigated since the start of the last century and a vast amount of literature and data are available on this subject. There are many factors influencing the breakdown voltage of gaseous insulation. Pressure, temperature, gas type, mixture components, electrode material, condition of electrode surface, contamination including dust and moisture, voltage duration, shape of voltage pulse, voltage frequency and polarity, gap geometry and size, electrode area, dielectric volume, etc. To improve the breakdown strength, from a designer's perspective, one should find an optimum set of values for all of the above variables. However, generally speaking, the thermodynamic state of gas, environmental factors, electrode configurations and applied voltage characteristics are imposed by practical conditions. Though various conditioning and coating of the electrodes can definitely improve the breakdown voltage, it is a major topic of vacuum breakdown studies. So, for gaseous insulation, we only focus on the following efforts to increasing the electrical strength: gas mixture and electrode material.

In high-voltage gas-filled systems and devices in which gases are used only for electrical insulation, the composition of a gas mixture is selected according to three criteria: maximum electric strength, high liquefaction temperature and minimal cost. The requirement for a nontoxic and nonaggressive mixture in the initial state and after exposure to discharges is also important. Under certain conditions, even a small quantity of SF_6 added to air or N_2 can appreciably increase their electric strength. According to [5], following exposure to $1.2/50 \mu\text{s}$ pulses, the breakdown voltage of the gap formed by a positive rod-plane electrode system filled with N_2 at $P < 0.3 \text{ MPa}$ increases by 60% after addition of 1% SF_6 . The opportunity to replace SF_6 and its mixtures with gas mixtures based on a less expensive gas or a gas ensuring higher electric strength in a mixture of other gases has also been studied. A promising way is addition of carbon dioxide to CCl_2F_2 [6].

C) Liquid

Efforts to understand breakdown mechanisms in a variety of liquid insulants have been continuing for many decades. However, unlike gases and solids, there is no single theory that has been unanimously accepted. This is because the molecular structure of liquids is not simple and not regular. In [7], information on short- and long-term electric strengths of dielectrics as functions of various influencing factors is presented. Methods of improving working field strengths and calculating the static, volt-second and statistical characteristics of the electric strength of insulation and the insulation service lifetime and reliability are also considered here. Factors influencing the electric strength include dielectric material properties and states (pressure, density, viscosity, temperature, molecular and supermolecular structures, mechanical stress condition, etc.), electrode material and state of the electrode surface, contaminations (solid particles, moisture, and gases dissolved in the liquid and adsorbed on the electrodes), polarity (for dc and impulse), type (for ac, frequency is also a factor) and duration (for pulses) of the voltage, insulation gap geometry and other environmental conditions.

It is often desirable to raise the hydrostatic pressure to increase the electric strength of liquids in the following cases: 1) for liquids with high electrical conductivity (water, glycerin, alcohol, etc.); 2) for large electrode areas (with more homogeneous field); and 3) for long voltage pulses ($>1 \mu\text{s}$). For very pure liquids under short-term voltage exposure, the main effect of temperature on electric strength is due to the temperature-dependent density. The electric strength slowly decreases with the increasing temperature. And the decrease in voltage duration weakens this effect. The dependence of electric strength on electrode material is perhaps due to the variations in the work function for electrons going from metals to liquids, the Young's modulus and thermodynamic characteristics. There was evidence that, the electric strength of liquid was mainly affected by the anode material. The increase in electric strength of cryogenic liquids with increased Young's modulus of electrodes was also revealed. Careful electrode degassing increases the electric strength of degassed liquids for dc and ac voltages by 15~20%. Shielding the electrode surface by ionic layers and heating the volume of liquid adjacent to micro-tips by high-voltage conduction currents are two means to increase local electrical conductivity and consequently increase the electric strength of gaps with liquid insulation. In some cases, the dependence of the electric strength of liquids on the dose or exposure time is displayed by a curve with a maximum. A transverse magnetic field hinders the multiplication of charge carriers and hence the onset of breakdown.

D) Solid

Solid dielectrics have higher breakdown strength compared to liquids and gases, but the conductivity is not negligible when the field exceeds about 10^5 V/cm, and it increases rapidly with field. Possible sources of conduction electrons are: Fowler-Nordheim field emission from electrodes, field aided thermionic emission (Schottky effect), and field enhanced ionization of impurities (Poole-Frenkel effect). Intuitively speaking, the improvement of solid breakdown strength can be ultimately reduced to inhibiting these effects. The main factors that influence the solid breakdown strength are: dielectric type and properties, thermodynamic and mechanical states, structural defects and impurities, electrode material and surface conditions, applied voltage, gap geometry, other environmental effects, etc.

Some recent articles published in the IEEE Transactions on Dielectrics and Electrical Insulation (1990-2009) present results, methods or implications for the improvement of solid insulation. Only a small fraction of the literature directly addresses the problem of improvement of breakdown strength of solid insulators, such as [8-10]. In [8], increased breakdown voltages were observed in thin (8 to 12 μm) commercial thermoplastic polymer films after they had been briefly exposed to low temperature, low pressure plasmas. This inexpensive and rapid gas treatment is a suitable method of increasing breakdown voltages in commercial polymer films. In [9], breakdown tests were conducted on a variety of polyethylenes and polypropylenes. High density polyethylene (HDPE) and polypropylene random copolymers (PPR) exhibited the highest breakdown strengths. Model cables insulated with HDPE were manufactured, and the impulse breakdown strength of the HDPE cables made under some specific manufacturing conditions was 1.6 times larger than that of conventional crosslinked polyethylene (XLPE). This improvement is perhaps due to the increased crystallinity of the insulating material, brought about by the heat annealing applied to the cable in a manufacturing process. In [10], electrical breakdown of plasma polymer films was studied by applying rectangular voltage pulses. The breakdown field increases after incorporation of fluorine atoms into the film when the pulse width is $< 5 \mu\text{s}$ due to the scattering of electronic carriers caused by C-F bonds.

Kerr Electro-Optic Field Mapping Using AC Modulation

The measurement setup consists of two main subsystems, optical and electrical, and a test cell (see Figure 2) with dielectric liquids and a pair of parallel plate electrodes inside as the intersection of the two subsystems. In our current experiments the vacuum pump, heating tape and oil filter are not used.

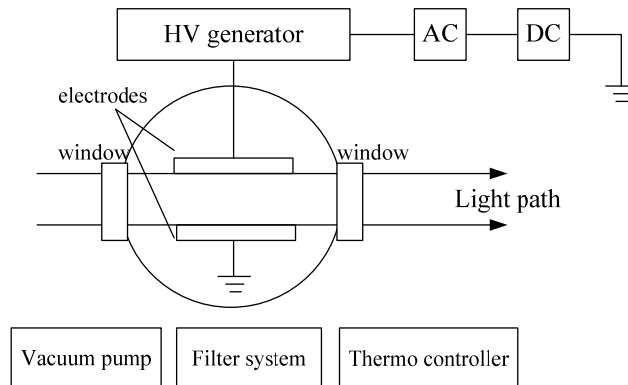


Figure 2. The test cell as the intersection of optical and electrical subsystems.

The optical subsystem: (1) Intensity-stabilized He-Ne laser is made by Melles Griot, model 05-STP-901. The diameter of the beam is 0.5 mm with wavelength of 632.8 nm, average power 1 mW and linearly polarized. It takes about 15 min for the laser to lock so that the output light intensity is stable. Any sort of reflection from optical components back into the laser head should be prevented. (2) The 20 \times beam expander is made by Special Optics. It expands the laser beam by 20 times so its diameter becomes 10 mm. For area measurements, two additional plano-convex lenses are placed in front of the beam expander to further expand the beam 4 times. The focal length of the first lens is 35 mm and that of the second one is 140 mm. The distance between the two lenses is 175 mm. The final beam diameter incident onto the CCD camera detector is 40 mm. (3) We use a linear polariscope configuration in which

no quarter wave plate is used. The three polarizers are made by Spindler&Hoyer with extinction ratio 500:1 and diameter of 3 inches. The first polarizer is used to attenuate the light to prevent saturation of the CCD camera. The angle of the transmission axis of the second polarizer is at 45° with respect to the vertical and that of the third one (analyzer) can be either 45° (aligned polariscope) or -45° (crossed polariscope). (4) A 35-105 mm, f/3.5-4.5 AF Nikon lens is mounted on the CCD camera via an adapter to focus the laser beam. When using the lens, the image of a 2 mm gap between the electrodes covers about 25 pixels. (5) The CCD (charge coupled device) camera is made by Andor Technology, model Ixon EM Plus. The image area is $8 \times 8 \text{ mm}^2$, active pixels 1004×1002 , pixel size $8 \mu\text{m}$. The quantum efficiency is typically 90% for the wavelength (6328. nm) we use. The CCD is cooled to -80°C . The electron multiplication technology enables that the camera can detect single photons. The unit for light intensity is count of electrons. The saturation level of each pixel is 50000 counts.

The electrical subsystem: The high voltage amplifier is made by Trek Inc., model 20/20, which amplifies a combined ac and dc signal generated by the function generator by 2000 times. The maximum input voltage 10 V corresponds to a maximum output of 20 kV. The output signal is connected to the feed-through on the top of the test cell. The function generator manufactured by Hewlett Packard, model 33120A, generates both ac and dc signals. To monitor voltage applied across the electrodes, we use a 1000:1 high-voltage probe made by Hewlett Packard, model 34111A.

We start from the linear polariscope, as shown in Figure 3.

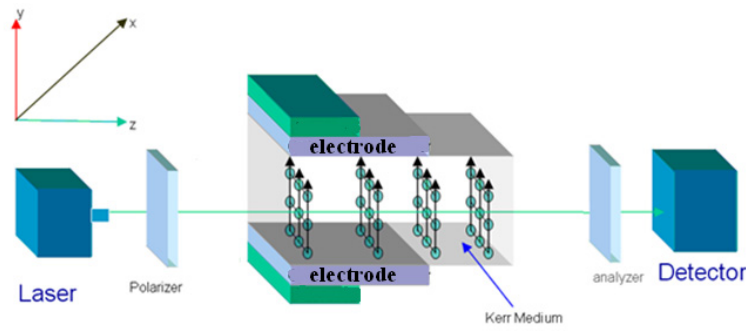


Figure 3. Illustrations of the linear polariscope for Kerr measurements.

The Jones matrix representation of light propagation through optical elements is a concise way to obtain the relation between the initial and final light intensities in Kerr electro-optical experiments. For polarizer (or analyzer), supposing the transmission axis is at angle θ with respect to the y-coordinate, we have:

$$\begin{pmatrix} e_x^{out} \\ e_y^{out} \end{pmatrix} = \begin{pmatrix} \cos \theta & \sin \theta \\ -\sin \theta & \cos \theta \end{pmatrix} \begin{pmatrix} 0 & 0 \\ 0 & 1 \end{pmatrix} \begin{pmatrix} \cos \theta & -\sin \theta \\ \sin \theta & \cos \theta \end{pmatrix} \begin{pmatrix} e_x^{in} \\ e_y^{in} \end{pmatrix} \equiv U_p(\theta) \begin{pmatrix} e_x^{in} \\ e_y^{in} \end{pmatrix} \quad (2)$$

For birefringent components, supposing the slow axis (the polarization direction of slow wave) is at angle ψ with respect to the y-coordinate and the slow wave is retarded by $\Delta\phi$ in phase, we have:

$$\begin{pmatrix} e_x^{out} \\ e_y^{out} \end{pmatrix} = \begin{pmatrix} \cos \psi & \sin \psi \\ -\sin \psi & \cos \psi \end{pmatrix} \begin{pmatrix} 1 & 0 \\ 0 & e^{-i\Delta\phi} \end{pmatrix} \begin{pmatrix} \cos \psi & -\sin \psi \\ \sin \psi & \cos \psi \end{pmatrix} \begin{pmatrix} e_x^{in} \\ e_y^{in} \end{pmatrix} \equiv U_b(\psi, \Delta\phi) \begin{pmatrix} e_x^{in} \\ e_y^{in} \end{pmatrix} \quad (3)$$

In a Kerr cell with electrode length along the light path of L and dielectric material Kerr constant denoted by B , we have a light phase shift of $\Delta\phi = 2\pi BLE^2$, where E is the applied HV electric field and in the direction of the slow axis. In the configuration of Figure 3, supposing the complex amplitude of the electric field of the linearly-polarized light is e_0 at the laser and e_l at the detector, we have:

$$\begin{pmatrix} e_{lx} \\ e_{ly} \end{pmatrix} = U_p(\theta_a) U_b(\psi_m, 2\pi BLE^2) U_b(\psi_q, \pi/2) U_p(\theta_p) \begin{pmatrix} e_{0x} \\ e_{0y} \end{pmatrix} \equiv \begin{pmatrix} A_{11} & A_{12} \\ A_{21} & A_{22} \end{pmatrix} \begin{pmatrix} e_{0x} \\ e_{0y} \end{pmatrix} \quad (4)$$

where the subscripts a , m , q and p represent analyzer, material, quarter-wave plate and polarizer, respectively. Further, if the polarization angle of the laser output is α (with respect to the y -axis, i.e., $\tan \alpha = \frac{e_{0x}}{e_{0y}}$), the intensity ratio is therefore:

$$\frac{I_1(E)}{I_0} = \frac{(e_{1x}^*, e_{1y}^*) \begin{pmatrix} e_{1x} \\ e_{1y} \end{pmatrix}}{(e_{0x}^*, e_{0y}^*) \begin{pmatrix} e_{0x} \\ e_{0y} \end{pmatrix}} = (\sin \alpha, \cos \alpha) \begin{pmatrix} |A_{11}|^2 + |A_{21}|^2 & A_{11}^* A_{12} + A_{21}^* A_{22} \\ A_{12}^* A_{11} + A_{22}^* A_{21} & |A_{12}|^2 + |A_{22}|^2 \end{pmatrix} \begin{pmatrix} \sin \alpha \\ \cos \alpha \end{pmatrix} \quad (5)$$

where I_0 is the incident light intensity from the laser. In general, this expression expanded in terms of the angles and basic parameters is very complicated. With the help of mathematical software, we can avoid such symbolic computation and easily obtain useful numerical results. Before demonstrating how we were led to a best experimental configuration, we should keep in mind the factors that will reduce the accuracy of the measurement: optical components not perfect or not precisely adjusted; impurities and flow of the dielectric liquid; fluctuations of laser intensity; thermal noise within the CCD camera; and environment. We should also estimate the requirements on the sensitivity in various configurations and the error in the presence of uncertainty and perturbation.

The Kerr constant of transformer oil is about $B = 2 \times 10^{-15} \text{ m/V}^2$, the breakdown strength is about $1.2 \times 10^7 \text{ V/m}$. If the dc electric field is $E_0 = 10^7 \text{ V/m}$, the electrode length is $L = 0.1 \text{ m}$, then we can estimate $\Delta\phi = 2\pi BLE_0^2 = 2\pi \times 2 \times 10^{-15} \times 0.1 \times (10^7)^2 \sim 0.1$ in radians. Similarly, for propylene carbonate, $B = 2 \times 10^{-12} \text{ m/V}^2$, the maximum field we can apply without over-current protection is $E_0 = 3 \times 10^5 \text{ V/m}$, we also have $\Delta\phi \sim 0.1$. However, when the voltage is applied, due to space charge, the field may not be uniform across the gap. If we want to measure the field distribution, we must at least be able to distinguish $0.9E_0$, E_0 and $1.1E_0$, that is, the measurement should detect the change of $\Delta\phi$ as small as 0.02. According to our measurements, it is observed that under low field (as is the case of propylene carbonate), the space charge distortion of electric field is large (up to 50%) only near electrodes; near the center of the gap, the distortion effect is relatively small, e.g. from $0.97E_0$ to $1.02E_0$. This imposes a much higher requirement for the sensitivity. For the measurement of such small signals, we have known from both numerical calculation and experimental observation that the contrast and error behavior of a linear polariscope is not adequate, so the next method we tried was to insert a quarter wave plate between the polarizer and the test cell (pre-semi polariscope). However, the pre-semi polariscope is also unsatisfactory, though its sensitivity and stability are much better than the linear polariscope. Because the laser output has slight fluctuations, the aforementioned methods often lead to inconsistent results. So finally, although the CCD technology has been greatly improved during the last decade, we still use ac modulation methods in our DC electric field experiments.

AC modulation is a smart approach to maximize measurement sensitivity for small Kerr constant materials. The frequency of the ac voltage superposed on the dc voltage should be high enough that the ac field does not disturb the space charge behavior in one cycle. For small Kerr constant material where $\Delta\phi \ll 1$, the linear polariscope with crossed polarizer (CP) configuration can approximate the intensity ratio by $\sin^2(\pi BLE^2) \approx \pi^2 B^2 L^2 E^4$. By simply increasing L or E , we can also improve the signal strength. However, this is usually not practical. We can further insert a single quarter wave plate between the polarizers to introduce an extra phase shift of $\pi/4$, then performing a Taylor series expansion and ignoring high order terms yields the intensity ratio $I_1(E)/I_0 = \sin^2(\pi BLE^2 + \pi/4) \approx 1/2 + \pi BLE^2$. If the total field is $\vec{E} = \vec{E}^{(dc)} + \vec{E}^{(ac)} \cos \omega t$, then:

$$\frac{I_1(E)}{I_0} \approx \frac{1}{2} + 2\pi BLE^{(dc)} E^{(ac)} \cos \omega t + \frac{\pi BL}{2} (E^{(ac)})^2 \cos 2\omega t \equiv \frac{I}{I_0} + \frac{I_\omega}{I_0} + \frac{I_{2\omega}}{I_0} \quad (6)$$

where the angle difference between the dc and ac voltage components is $\Delta\Phi = 0$, $I_\omega = KE^{(dc)}E^{(ac)}$, $I_{2\omega} = \frac{1}{4}K(E^{(ac)})^2$, and K is a proportionality coefficient to be determined from measurements according to the method described next.

If the transmitted light at a single point is detected by a photo diode, a lock-in amplifier is used to measure the first and second harmonics based on which the dc and ac field components can be calculated. A lock-

in amplifier is a type of amplifier that provides a dc output proportional to the ac signal amplitude under investigation. It works by multiplying the input signal with the reference ac signal and integrating it over a specified time. The resulting signal is an essentially dc signal, where the contribution from any signal that is not at the same frequency as the reference signal is attenuated essentially to zero. If we use the CCD camera to simultaneously record the transmitted light intensity in an area, signal processing techniques should be adopted to replace the function of the lock-in amplifier.

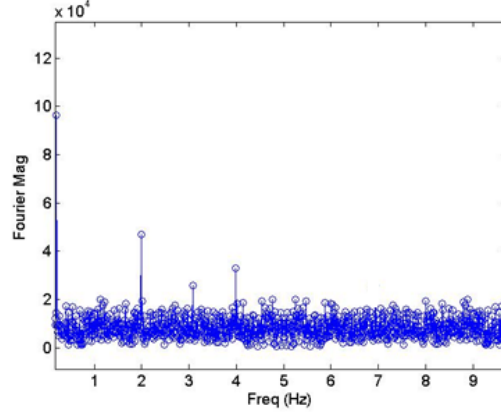


Figure 4. FFT of the recorded time series of light intensity at a point between the electrodes with dc voltage of 300 V and ac modulation of 2 Hz.

The sampling frequency and the total frame number of the CCD camera are set to be 30 Hz and 200. We conduct the measurements using ac modulation at 2 Hz. The dc voltage is 300 V and the 2-mm gap is filled with high Kerr constant propylene carbonate. There are about 25 pixels between the electrodes. Thus, for each pixel, we obtain a time sequence of length 200. We want to extract the components corresponding to fundamental frequency 2 Hz and double frequency 4 Hz. The data processing in MATLAB is straightforward. In Figure 4 (the 3Hz component is due to noise), the FFT of the recorded time series of light intensity at a point between the electrodes is shown, from which the ratio of fundamental frequency and double frequency components can be determined.

For each point along a line connecting the two electrodes, I_ω and $I_{2\omega}$ can be obtained from the output of CCD camera, so $E^{(dc)} = \frac{I_\omega}{2\sqrt{KI_{2\omega}}}$. According to the additional condition that $\int_0^L E^{(dc)} dx = U$, we can determine the coefficient K and therefore the dc field distribution.

We completed a set of measurements using ac modulation at 2 Hz. The dc voltages (U) are 300 V (for stainless steel, it's 200 V), and the $L=2$ mm gap is filled with propylene carbonate. There are about 25 pixels between the electrodes. Here 'a set' means various upper electrodes with the same bottom electrode (#2, stainless steel). The polarity of the applied voltage can also be switched. We plan measurements using 25 different electrodes with various materials of copper, brass, bronze, aluminum, stainless steel, steel, iron and titanium. In the measurements, we labeled the data in the following manner: "n02p21" stands for the cathode (n), is made of material #2, and the anode (p) of material #21. We only give some representative results in the following.

As indicated by Figure 5(a), alloy contents (#10-14 are all aluminum alloys) and the different electrode surface treatments make insignificant contributions perhaps because the electric field is relatively low in the measurement. In Figure 5(b), comparison among different anode electrode materials suggests: (1) aluminum at anode results in minimum field near anode; (2) near cathode (copper), the normalized field intensity does not vary too much (around 1.15).

Propylene carbonate is reactive with some materials like iron and steel, generating particle layers on the electrodes. When the field is applied the particle motion caused irregular liquid flow, thus the light intensity fluctuated and the detected SNR becomes very small (in most cases, it yields no reasonable result). However, taking #21 stainless steel as example, there seems to be bipolar homo-charge injection

and therefore the field intensity near both electrodes is reduced, as shown in Figure 5(c). However, this result lacks of consistency.

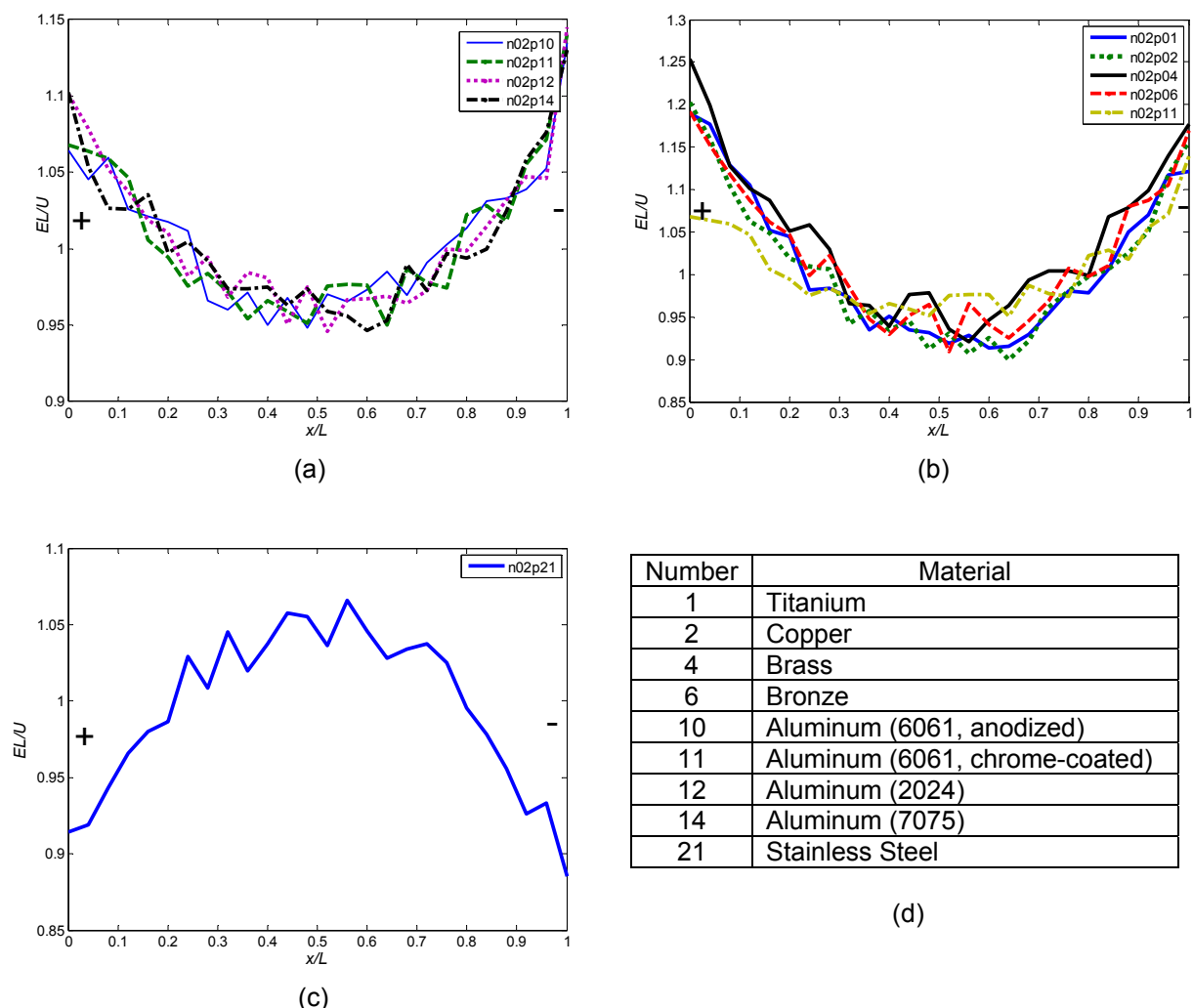


Figure 5. Comparisons of field distributions (a-c) measured with copper(#2) as cathode at $x/L=1$ and various other materials listed in (d) as anode at dc voltage of 300 V and 2 Hz ac modulation.

Space Charge Effects in High-Voltage Pulsed Propylene Carbonate

The Kerr electro-optic field mapping technique has been used to study space charge effects in HV pulsed propylene carbonate in stainless steel parallel-plane electrodes in [11]. The light intensity was recorded on Polaroid film. Our new results to be presented here, compared with those in past literature, have much higher spatial resolution and accuracy due to the use of the CCD camera; also the electronic shutter in the CCD realizes much better synchronization than the mechanical shutter used in previous experiments. We further improved measurement sensitivity by removing the Nikon lens, which increases spatial resolution to about 500 pixels across the 5 mm gap with about 5000 signal electrons at each pixel. This allows reduced exposure time from ~ 1 ms to 10 μ s.

Our data can be divided into three parts: 1). For the same pair of electrodes and the same peak HV value, record the dynamics of charge injection under both HV polarities. 2). For the same pair of electrodes and various peak HV values (both polarities), measure the distributions of electric field and space charge density in the gap at the same instant (very close to peak time of the HV; because the triggering of the Marx generator does not yield exactly the same waveform each time, the peak time itself varies slightly). 3). For various pairs of electrodes and the same peak HV value (both polarities), measure the distributions of electric field and space charge density in the gap at the same instant (only the top electrode was replaced). This part of the experiment is still ongoing.

We base our measurements on the pre-semi polariscope. Usually, the y -axis is so chosen that it coincides with the direction of applied HV field, i.e. $\psi_m = 0$. In the experiment, we also let $\psi_q = 0$, $\theta_p = \alpha = \pi/4$ and $\theta_p - \theta_a = \pi/2$ (crossed polarizers) so that the light intensity as a function of electric field is:

$$\frac{I_1(E)}{I_0} = \frac{1 + \sin(2\pi BLE^2)}{2} \quad (7)$$

When there is no electric field, i.e., $E = 0$, the output light intensity is $I_1(0) = I_0/2$. Thus, we obtain the relation between the output intensity after and before HV application:

$$\sin(2\pi BLE^2) = \frac{I_1(E)}{I_1(0)} - 1 \quad (8)$$

According to this relation, if the electric field is known, one can predict the distribution of the detected light intensity. However, in the measurement the CCD camera can record $I_1(0)$ and $I_1(E)$ at each point between two electrodes. We need to solve for the corresponding electric field:

$$2\pi BLE^2 = 2k\pi + \arcsin\left[\frac{I_1(E)}{I_1(0)} - 1\right] \text{ or } 2\pi BLE^2 = (2k'+1)\pi - \arcsin\left[\frac{I_1(E)}{I_1(0)} - 1\right] \quad (9)$$

There seems to be an infinite number of solutions, while only one of them is real. Considering the electric field distribution along the central line in the gap, two conditions should be satisfied: (1) the profile of the electric field should be continuous (and more rigorously, differentiable, since the derivative of electric field is proportional to the space charge density); and (2) the integration of the electric field along the line equals to the instantaneous voltage applied to the electrodes. The first condition implies that the electric field varies continuously around the mean field in the gap $E_{av} = U_{inst} / D$ where U_{inst} is the instantaneous voltage and D is the width of the electrode gap. Therefore, the value of k or k' should be so chosen that the corresponding E falls in an interval which contains E_{av} . When the absolute values of $\sin(2\pi BLE^2)$ at all points are smaller than 1, the above-mentioned method can uniquely determine an electric field distribution.

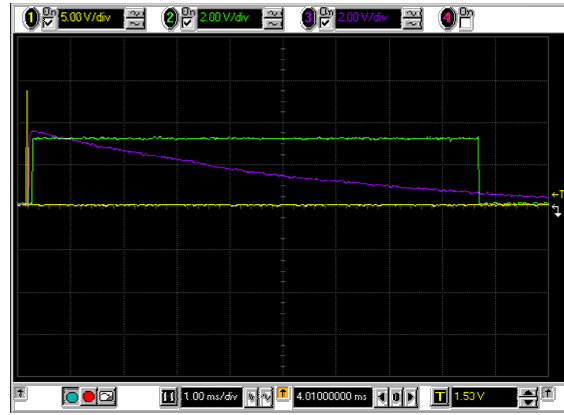


Figure 6. Waveform of triggering pulses for impulse generator (channel 1: yellow) and CCD camera (channel 2: green) and high voltage pulse measured by the capacitive divider (Channel 3: purple).

The experimental configuration is: pre-semi polariscope (a $\frac{1}{4}\lambda$ plates between polarizer and test cell) with crossed polarizers; electrode material: Cu (top, HV) and Al (bottom, grounded); $D=5$ mm gap; CCD exposure time is $10 \mu s$. The waveform captured by the oscilloscope is shown in Figure 6. Channel 1: 15 V pulse to trigger Marx generator (at $t=0$); Channel 2: TTL high level signal to trigger CCD camera; Channel 3: HV measured by 5068:1 capacitive divider (the duration of HV pulse is ~ 10 ms and the peak voltage ~ 18 kV appears at about $t=0.1$ ms).

The light intensity pictures were analyzed along a line between electrodes in the center of the electrode gap. In Figure 7, the distributions of light intensity, electric field and space charge density under various high voltages of positive polarity at the top $x = 0$ copper electrode are presented.

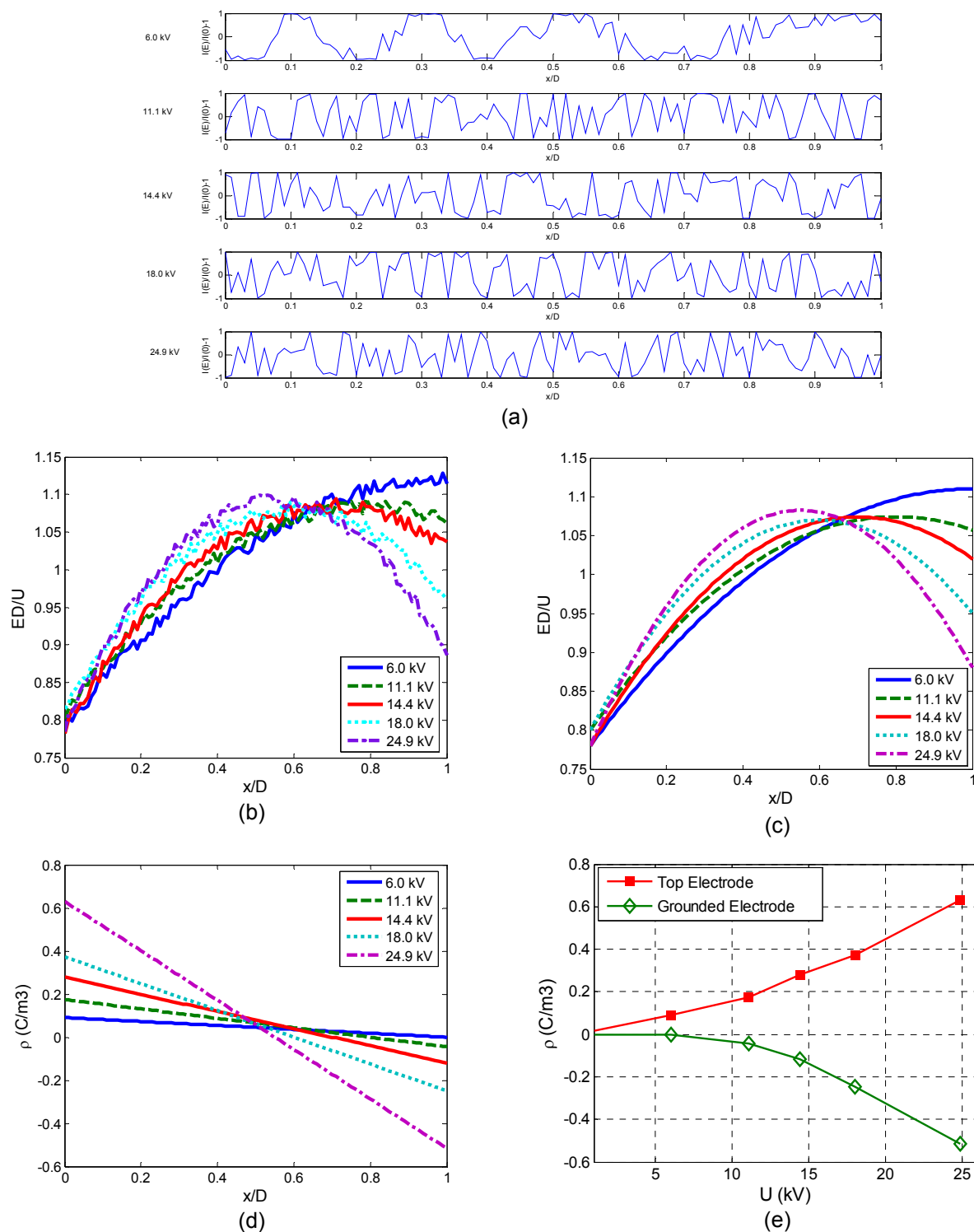


Figure 7 Pulsed high voltage measurements of electric field and space charge density distributions in propylene carbonate. (a) Measured light intensity for various high voltages, (b) measured and (c) smoothed electric field and (d) space charge distributions along the central line between the electrodes of the gap under various positive-polarity high voltages, where $x=0$ corresponds to the top electrode (Copper anode) and $x=D$ corresponds to the ground electrode (Aluminum cathode). (e) The charge density at the top and bottom electrodes for various applied voltages.

In Figure 7(a), it is clear that there are multiple “maxima” and “minima” across the gap. However, not all of them correspond to a “fringe” as appearing in previous publications using Polaroid film. From the light intensity distribution for the parallel-plane electrodes, the electric field is calculated as a function of position, as shown in Figure 7(b). The field profiles are noisy, which may be attributed to various factors causing fluctuations in experimental measurements. Therefore the measured data was smoothed using a quadratic fit which is plotted in Figure 7(c). The space charge distributions in Figure 7(d) calculated from Figure 7(c) according to Gauss’ law with propylene carbonate relative dielectric constant of 65 show positive (negative) charge injections from the anode (cathode). This is the case of homocharge injection in Figure 1(c), in which the electric field near the anode is reduced to about 80% of the average field under all applied voltages. In Figure 7(e), local charge densities at both electrodes versus applied high voltage are revealed. The correlation is not the linear one assumed in many analytical models. Also the charge injecting capability of the anode where HV is applied is stronger than that of the grounded cathode.

Similarly we have the results under negative polarity high voltages, as shown in Figure 8. The space charge distributions in Figure 8(b) calculated from the smoothed field profile in Figure 8(a) show positive (negative) charge injections from the anode (cathode). This is the case of unipolar charge injection in Figure 1(b), and the electric field near the cathode (anode) is reduced (enhanced). In Figure 8(c), we plot local charge densities at both electrodes versus applied high voltage. It is interesting that when the HV polarity reverses, the charge injection mode changes from bipolar to unipolar.

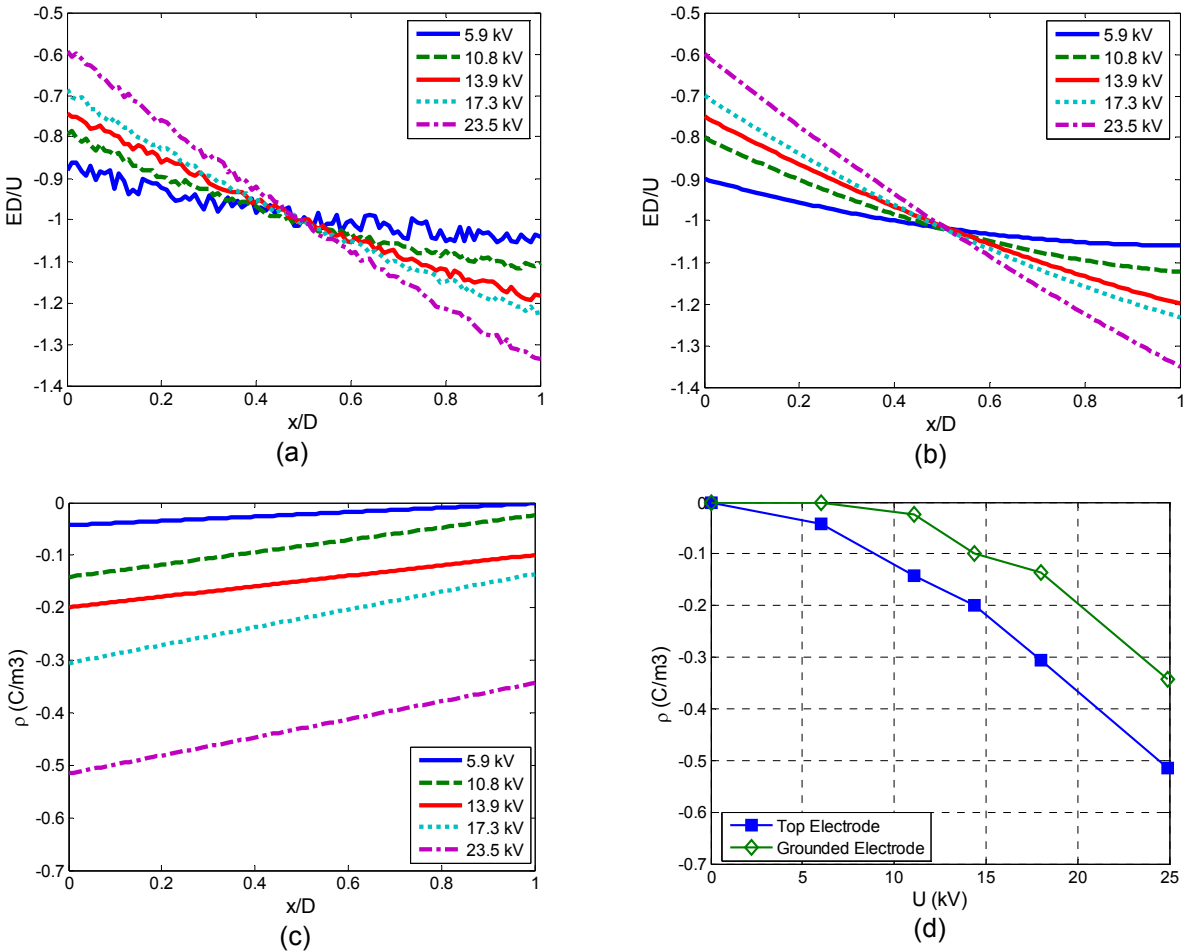


Figure 8. Electric field and space charge distributions along the central line of the gap with reverse polarity from Figure 7 under various negative-polarity high voltages, where $x=0$ corresponds to the top electrode (cathode).

References

- [1] M. Zahn, Y. Ohki, D. B. Fenneman, R. J. Gripshover, and V. J. Gehman, Jr., "Dielectric Properties of Water and Water/Ethylene Glycol Mixtures for Use in Pulsed Power System Design," *Proc. of the IEEE*, V. 74, pp. 1182-1221, 1986.
- [2] M. Zahn, "Optical, Electrical and Electromechanical Measurement Methodologies of Field, Charge and Polarization in Dielectrics," *IEEE Transactions on Dielectrics and Electrical Insulation*, Vol. 5, No. 5, pp. 627-650, October 1998.
- [3] K. W. Arnold, R. B. Britton, S. C. Zanon, et al., "Electrical Breakdown between a Sphere and a Plane in Vacuum," in *Proc. 6th Int. Conf. on Ionization Phenomena in Gases*, vol. 2, pp. 101-107, 1963.
- [4] L. T. Pranevichyus and I. Y. Bartashyus, "Mechanism for Electrical Breakdown in High Vacuum," *Sov. Phys. Tech. Phys.*, vol. 14, 1301-1302, 1970.
- [5] N. H. Malik, A. A. Al-Arainy and M. I. Qureshi, *Electrical Insulation in Power Systems*, New York: Marcel Dekker, 1998.
- [6] A. H. Cookson and B. O. Pederson, "Analysis of the High-Voltage Breakdown Results for Mixtures of SF₆ with CO₂, N₂ and Air," in *Proc. 3rd Symp. on High-Voltage Engineering*, pp. 31/13/1-31/13/4, 1979.
- [7] V. Y. Ushakov, *Insulation of High-Voltage Equipment*, Berlin/Heidelberg: Springer-Verlag, 2004.
- [8] M. Binder, W. L. Wade, P. Cygan, et al., "Breakdown Voltages of Commercial Polymer Films Following Exposure to Various Gas Plasmas," *Electrical Insulation, IEEE Transactions on*, vol.27, no.2, pp.399-401, Apr 1992.
- [9] T. Niwa, M. Hatada, H. Miyata, et al., "Studies on the Improvement of Breakdown Strength of Polyolefins," *Electrical Insulation, IEEE Transactions on*, vol.28, no.1, pp.30-34, Feb 1993.
- [10] T. Nakano, M. Fukuyama, H. Hayashi, et al., "Effect of Polar Groups on the Electrical Breakdown Strength of Plasma-Polymerized Films," *Electrical Insulation, IEEE Transactions on*, vol.25, no.6, pp.1085-1091, Dec 1990.
- [11] A. Helgeson and M. Zahn, "Kerr Electro-Optic Measurements of Space Charge Effects in HV Pulsed Propylene Carbonate," *IEEE Transactions on Dielectrics and Electrical Insulation*, Vol. 9, No. 5, pp. 838-844, October 2002.

5. Continuum Modeling of Micro-particle Electrorotation in Couette and Poiseuille Flows

Sponsors

This work was sponsored by the National Science Council (Taipei, Taiwan) through the Taiwan Merit Scholarships and by the United States-Israel Binational Science Foundation (BSF).

Project Staff

Hsin-Fu Huang and Markus Zahn

Research Collaborators

Prof. Elisabeth Lemaire, Laboratoire de Physique de la Matière Condensée, CNRS-Université de Nice-Sophia, Antipolis, 06108 Nice cedex 2, France

Prof. Mark I. Shliomis is with the Department of Mechanical Engineering at the Ben-Gurion University of the Negev, P.O. Box 653 Beer-Sheva 84105, Israel.

Introduction

A classical continuum mechanical model is developed to analyze the flow phenomena and negative electro-rheological (ER) responses of a dilute particle-liquid mixture (or ER fluid) with the suspended solid micro-particles undergoing spontaneous electrorotation induced by an externally applied direct current (DC) electric field in both two dimensional Couette and Poiseuille flow geometries.

Recent experimental observations found that: (i) with a given constant shear rate or equivalently the Couette boundary driving velocity, the measured shear stress required to drive the Couette ER fluid flow is reduced (an effectively decreased viscosity) [1] and (ii) at a given constant pressure gradient, the Poiseuille flow rate of the ER fluid can be increased [2] both by applying a uniform DC electric field perpendicular to the direction of the flows. The mechanism responsible for the apparent increased flow rate or decreased effective viscosity, i.e., negative ER effect, was attributed to the spontaneous electrorotation of the dielectric micro-particles suspended within the carrier liquid, which is a mechanism different from the traditional electrophoresis or electromigration phenomenon as mentioned in previous negative ER literature [3]-[4]. This spontaneous particle rotation under the action of a DC electric field is often called the “Quincke rotation” for von G. Quincke’s systematic study done in 1896 [5]-[10].

Quincke rotation characterizes the spontaneous electrorotation of dielectric insulating particles immersed in a more conducting liquid phase when subjected to a DC electric field. Due to the electrical property mismatch between the two phases, the Maxwell-Wagner polarization induced dipole moment on the particles is in the opposite direction to that of the applied field, which is in general an unstable condition. As the applied DC field exceeds a threshold strength, the liquid viscous torque can no longer withstand small perturbations in the electrical torque exerted on the particles, thus the instability grows and the particles start to rotate in a self-sustaining manner. The threshold electric field strength is given by [9]-[10]

$$E_c \equiv \left(1 + \frac{\sigma_2}{2\sigma_1}\right) \sqrt{\frac{8\eta_0\sigma_1}{3\varepsilon_1\sigma_2(\tau_2 - \tau_1)}}, \quad (1)$$

where η_0 , ε_1 , and σ_1 are respectively the viscosity, permittivity, and conductivity of the carrier liquid; ε_2 and σ_2 are the respective permittivity and conductivity of the solid micro-particles; τ_1 and τ_2 are the respective charge relaxation times of the liquid and solid phases defined as $\tau_i = \varepsilon_i / \sigma_i$ for each phase. Note that the threshold electric field strength will be real valued only when $\tau_2 > \tau_1$, i.e., the liquid has a charge relaxation time less than that of the solid phase. For this work, we consider the material combination of $\varepsilon_1 \sim \varepsilon_2$ and $\sigma_1 > \sigma_2$ as shown in Figure 1.

Although models are given in current literature [1]-[2], [11]-[14] for analyzing the present negative ER phenomenon, most of them are focused on the dynamics of a single particle and the utilization of a two-phase effective continuum description [15]. Little has been done in developing a continuum mechanical

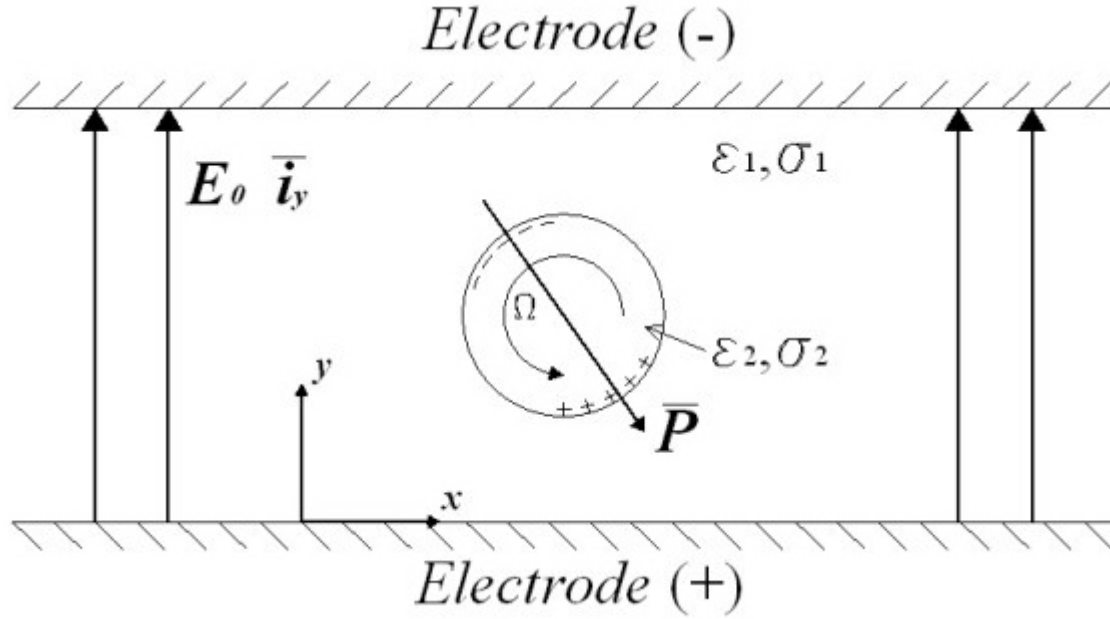


Figure 1: Spontaneous Quincke electrototation of insulating particles suspended in a slightly conducting liquid subjected to a DC electric field with the field strength exceeding the critical value given by (1).

model from a more classical, field theory based perspective in predicting the dynamical behavior of fluids consisting of micro-particles undergoing spontaneous electrorotation. To the best of the authors' knowledge, the ferrofluid spin-up flow problem is the most representative flow phenomenon arising from internal particle rotation in current rheology research [16]. In a ferrofluid spin-up flow, magnetic torque is introduced into the ferrofluid, which consists of colloidally stabilized magnetite nanoparticles suspended in a non-magnetizable liquid, through the misalignment of the particle's permanent magnetization and the applied rotating magnetic field. From a macroscopic point of view, the introduced magnetic torque manifests itself through the ensemble of the particle-liquid interactions as the antisymmetric component of the continuum stress tensor while the average effect of the internal particle rotation is reflected in the macro, continuum fluid hydrodynamic spin. In order to describe how particle rotation affects the continuum flow motion, an angular momentum conservation equation is added and coupled with the linear momentum equation so that, in general, the externally applied magnetic body couple, angular momentum conversion between linear and spin velocity fields, and the diffusive transport of angular momentum are incorporated into the description of the flow momentum balances [16]-[21].

Governing Equations

After identifying the mathematically parallel, physically analogous mechanisms that govern the respective dynamics of electrorotation and ferrofluid spin-up flows, we combine the theories of particle electromechanics and continuum antisymmetric stresses to formulate the governing equations that describe the electro-quasi-static (EQS) and fluid dynamical aspects of this negative ER phenomenon. The full governing equations in their most general forms are:

(i) Gauss' Law for the displacement field and the EQS Faraday's Law [8],

$$\nabla \cdot \bar{D} = \rho_f, \quad (2)$$

$$\nabla \times \bar{E} \approx 0, \quad (3)$$

(ii) the polarization relaxation equation [20],

$$\frac{D\bar{P}}{Dt} = (\bar{\Omega} \times \bar{P}) - \frac{1}{\tau_{MW}} (\bar{P} - \bar{P}_{eq}), \quad (4)$$

(iii) the continuity equation or conservation of mass for incompressible flows,

$$\nabla \cdot \bar{v} = 0, \quad (5)$$

(iv) the linear momentum equation,

$$\rho \frac{D\bar{v}}{Dt} = -\nabla p + (\bar{P} \cdot \nabla) \bar{E} + 2\zeta \nabla \times \bar{\omega} + \beta \nabla (\nabla \cdot \bar{v}) + \eta_e \nabla^2 \bar{v} \quad (6)$$

and (v) the angular momentum equation,

$$I \frac{D\bar{\omega}}{Dt} = \bar{P} \times \bar{E} + 2\zeta (\nabla \times \bar{v} - 2\bar{\omega}) + \beta' \nabla (\nabla \cdot \bar{\omega}) + \eta' \nabla^2 \bar{\omega}, \quad (7)$$

where \bar{D} is the displacement field, \bar{E} is the electric field, ρ_f is the free space charge density, \bar{P} is the macro scale fluid polarization, $\bar{\Omega}$ is the micro scale particle rotation velocity, \bar{P}_{eq} is the equilibrium polarization for charge relaxation, τ_{MW} is the Maxwell-Wagner relaxation time given as $\tau_{MW} = (2\varepsilon_1 + \varepsilon_2) / (2\sigma_1 + \sigma_2)$ for a spherical particle, \bar{v} is the macro scale linear velocity field, $\bar{\omega}$ is the macro scale fluid hydrodynamic spin velocity, ρ is the ER fluid density, I is the averaged moment of inertia, p is the pressure in the flow field, η' is the spin viscosity, ζ is the vortex viscosity and is related to the particle solid fraction, ϕ , and carrier liquid viscosity, η_0 , through $\zeta \approx 1.5\phi\eta_0$, $\eta_e = \zeta + \eta$ is the sum of the vortex viscosity and the zero field ER fluid viscosity where $\eta \approx \eta_0(1 + 2.5\phi)$, $\beta = \lambda + \eta - \zeta$ is the sum of the second coefficient of viscosity, λ , the zero field ER fluid viscosity, and the negative of the vortex viscosity, and $\beta' = \eta' + \lambda'$ is the sum of the spin viscosity and the second coefficient of spin viscosity, λ' [15]-[18].

With the assumptions of an electrically neutral system, a dilute mixture, neutrally buoyant particles, two-dimensional geometry, and steady fully developed viscous flow, the full governing equations are then simplified for both Couette and Poiseuille flow cases. The boundary conditions applied are the no-slip and free-to-spin boundary conditions on the linear and spin velocity fields, respectively. Using symbolic calculation packages, the two sets of equations are solved to obtain analytical expressions in the zero spin viscosity limit, i.e., $\eta' = 0$, for the negative ER phenomena discussed herein.

Parametric studies are performed to analyze (i) the variations of the effective viscosity with respect to the applied shear rate and electric field strength for Couette flow, and (ii) the variations of the apparent flow rate with respect to the applied pressure gradient and electric field strength for Poiseuille flow as described in Figure 2. Preliminary results show that with a DC electric field strength higher than the Quincke threshold applied perpendicularly to the flow direction, the spin velocity (or ER fluid rotation) is increased and the effective viscosity is decreased as compared to the zero electric field value of the ER fluid viscosity for Couette flow at a given driving shear rate. Moreover, it is also found that with a constant driving pressure gradient, the spontaneous internal particle electrorotation generally enhances the ER fluid rotation as well as the flow velocity and the subsequent volume flow rate of Poiseuille flow when the applied DC field perpendicular to the direction of flow has a strength higher than the critical strength for the onset of Quincke rotation as compared to the zero field results. The classical continuum mechanical (field theory based) solutions to the effective viscosity and volume flow rate in the zero spin viscosity limit presented in this work are generally consistent with those obtained from two-phase effective continuum models (single particle based) and experimental observations as found in current literature [1]-[2], [11]-[14].

Additional to offering complementary insights to the analogous ferrofluid spin-up problem, future work on this topic includes a more advanced modeling of the polarization relaxation processes in the ER fluid flow, the investigation of finite spin viscosity effects on the angular momentum balances within the flow field, and the search of possible practical applications for such novel negative ER phenomenon [22].

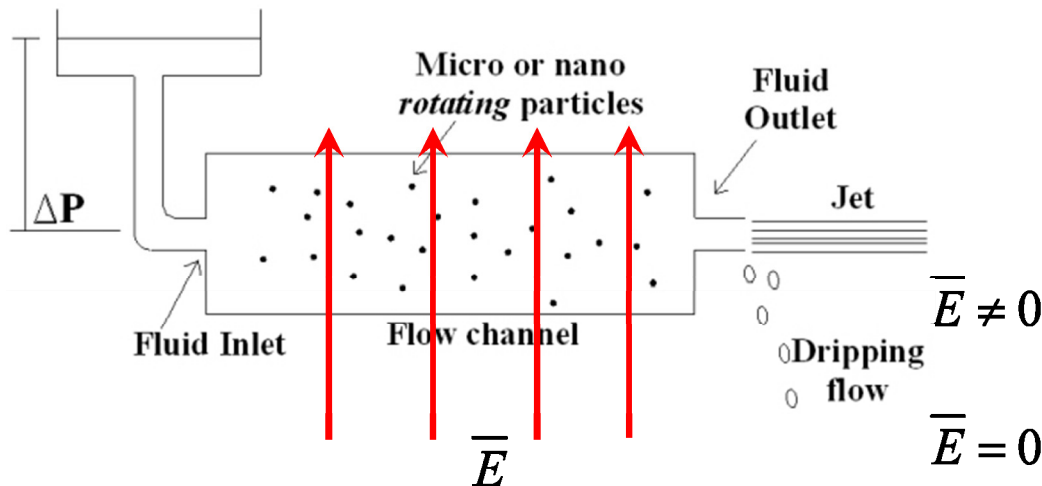


Figure 2. Experiments have shown that for a given pressure gradient, the Poiseuille flow rate can be increased by introducing a micro-particle rotation to the fluid via the application of an external electric field greater than the threshold electric field of (1) [2].

References

- [1] L. Lobry and E. Lemaire, "Viscosity Decrease Induced by a DC Electric Field in a Suspension," *Journal of Electrostatics*, Vol. 47, pp.61-69, 1999.
- [2] E. Lemaire, L. Lobry, and N. Pannacci, "Flow Rate Increased by Electrorotation in a Capillary," *Journal of Electrostatics*, Vol. 64, pp.586-590, 2006.
- [3] J.N. Foulc, P. Atten, and N. Felici, "Macroscopic Model of Interaction between Particles in an Electrorheological Fluid," *Journal of Electrostatics*, Vol. 33, pp.103-112, 1994.
- [4] C.W. Wu and H. Conrad, "Negative Electrorheological Effect and Electrical Properties of a Teflon/silicone Oil Suspension," *Journal of Rheology*, Vol. 41(2), pp.267-281, 1997.
- [5] G. Quincke, "Ueber Rotationen im Constanten Electricischen Felde," *Annalen der Physik und Chemie*, Band 59(11), pp.417-486, 1896 (in German).
- [6] J.R. Melcher and G.I. Taylor, "Electrohydrodynamics: a Review of the Role of Interfacial Shear Stresses," *Annual Review of Fluid Mechanics*, Vol. 1, pp.111-146, 1969.
- [7] J.R. Melcher, "Electric Fields and Moving Media," *IEEE Transactions on Education*, Vol. E-17(2), pp.100-110, 1974.
- [8] J.R. Melcher, *Continuum Electromechanics*, Cambridge, MA: MIT Press, 1981, Sec. 5-14.
- [9] T.B. Jones, "Quincke Rotation of Spheres," *IEEE Transactions on Industry Applications*, Vol. IA-20(4), pp.845-849, 1984.
- [10] T.B. Jones, *Electromechanics of Particles*, New York, NY: Cambridge University Press, 1995, pp.98-100.
- [11] A. Cebers, E. Lemaire, and L. Lobry, "Flow Modification Induced by Quincke Rotation in a Capillary," *International Journal of Modern Physics B*, Vol. 16(17-18), pp.2063-2069, 2002.
- [12] A. Cebers, E. Lemaire, and L. Lobry, "Internal Rotations in Dielectric Suspensions," *Magnetohydrodynamics*, Vol. 36(4), pp.347-364, 2000.
- [13] N. Pannacci, E. Lemaire, and L. Lobry, "Rheology and Structure of a Suspension of Particles Subjected to Quincke Rotation," *Rheologica Acta*, Vol. 46, pp.899-904, 2007.
- [14] E. Lemaire, L. Lobry, N. Pannacci, and F. Peters, "Viscosity of an Electro-rheological Suspension with
- [15] Internal Rotations," *Journal of Rheology*, Vol. 52(3), pp.769-783, 2008.

- [16] H. Brenner, "Rheology of Two-phase Systems," *Annual Review of Fluid Mechanics*, Vol. 2, pp.137-176, 1970.
- [17] R.E. Rosensweig, *Ferrohydrodynamics* (reprint edn.), Mineola, NY: Dover Publications, 1997, pp.237-271.
- [18] J.S. Dahler and L.E. Scriven, "Angular Momentum of Continua," *Nature*, Vol. 192, pp.36-37, 1961.
- [19] D.W. Condiff and J.S. Dahler, "Fluid Mechanical Aspects of Antisymmetric Stress," *Physics of Fluids*, Vol. 7(6), pp.842-854, 1964.
- [20] A.C. Eringen, "Theory of Micropolar Fluids," *J. Math. Mech.*, Vol. 16(1), pp.1-16, 1966.
- [21] A. O. Cebers, "Internal Rotation in the Hydrodynamics of Weakly Conducting Dielectric Suspensions," *Mekhanika Zhidkosti i Gaza*, Vol. 2, pp.86-93, 1980 (in Russian).
- [22] H-F Huang, M. Zahn, and Elisabeth Lemaire, "Continuum Modeling of Micro-particle Electrorotation in Couette and Poiseuille Flows-The Zero Spin Viscosity Limit", *Journal of Electrostatics* 68, pp. 345-359, 2010.

Publications

- [1] J. G. Hwang, M. Zahn, F. M. O'Sullivan, L. A. A. Pettersson, O. Hjortstam, and R. Liu, "Effects of nanoparticle charging on streamer development in transformer oil- based nanofluids," *J. Appl. Phys.*, vol. 107, no. 1, pp. 014310-1 – 014310-17, Jan. 2010.
- [2] J. G. Hwang, M. Zahn, F. M. O'Sullivan, L. A. A. Pettersson, O. Hjortstam, and R. Liu, "Electron scavenging by conductive nanoparticles in oil insulated power transformers," in *2009 Joint Electrostatics Conference*, Boston, MA, USA, Jun. 2009, pp. 1-12 (Invited).
- [3] J. G. Hwang, M. Zahn, L. A. A. Pettersson, O. Hjortstam, and Rongsheng Liu, "Modeling streamers in transformer oil: the transitional fast 3rd mode streamer," in *Proc. IEEE 9th Int. Conf. Prop. Appl. Dielectr. Mat., ICPADM 2009*, Harbin, China, Jul. 2009, pp. 573-578.
- [4] J. G. Hwang. Elucidating the mechanisms behind pre-breakdown phenomena in transformer oil systems. PhD dissertation, Massachusetts Institute of Technology, Cambridge, MA, USA, 2010.
- [5] J. Jadidian, J. G. Hwang, M. Zahn and L. A. A. Pettersson, "Charge Transport Mechanisms in Liquid-Solid Insulation Systems, " To be presented at IEEE International Conference on Liquid Dielectrics, Trondheim, 2011.
- [6] H-F Huang, M. Zahn, E. Lemaire, and M.I. Shliomis, "Continuum modeling of micro-particle electrorotation in Couette and Poiseuille flows-the zero spin viscosity limit," 2009 Electrostatics Joint Conference, Paper 1.3 (June 16-18, 2009, Boston University).